Alongshore variability in crescentic sandbar patterns at a strongly curved coast

J Rutten, B Dubarbier, T D Price, B G Ruessink, Bruno Castelle

Alongshore variability in crescentic sandbar patterns at a strongly curved coast

J. Rutten[1], B. Dubarbier[3], T. D. Price[2], B. G. Ruessink[2], B. Castelle[4]

[1]Laboratorio de Ingeniería y Procesos Costeros, Instituto de Ingeniería, Universidad Nacional Autónoma de México, Sisal, México

[2]Department of Physical Geography, Faculty of Geosciences, Utrecht University, PO Box 80115, 3508 TC Utrecht, The Netherlands

[3]Université de Bordeaux, UMR EPOC, Bordeaux, France

[4]CNRS, UMR EPOC, Pessac, France

Key Points:

- Curved coasts impose an alongshore variation in wave incidence, provoking variability in the formation of crescentic sandbar patterns
- Crescentic sandbar patterns develop where alongshore currents and refraction-induced wave height reduction are limited
- Implementing a km-scale coastline perturbation may increase local near-normal wave incidence and thereby the presence of rip currents

Corresponding author: Jantien Rutten, jrutten@iingen.unam.mx

Abstract

Sandbars, submerged ridges of sand parallel to the shoreline, tend to develop crescentic patterns while migrating onshore. At straight coasts, these patterns form preferably under near-normal waves through the generation of circulation cells in the flow field, whereas they decay under energetic oblique waves with associated intense alongshore currents. Recently, observations at a man-made convex curved coast showed an alongshore variability in patterning that seems related to a spatiotemporal variability of the local wave angle (Sand Engine). Here, we aim to systematically explore how coastline curvature contributes to alongshore variability in crescentic pattern formation, by introducing local differences in wave angle and the resulting flow field. A non-linear morphodynamic model was used to simulate the patterns in an initially alongshore uniform sandbar that migrates onshore along the imposed curved coast. The model was forced by a time-invariant and time-varying offshore wave angle. Simulations show that the presence of patterns and their growth rate relate to the local breaker angle, depending on the schematisation of the offshore angle and the local coastline orientation. Growth rates decrease with increasing obliquity as both refraction-induced reductions of the wave height as well as alongshore currents increase. Furthermore, simulations of variations in coastline curvature show that patterns may develop faster at strongly curved coasts if this curvature leads to an increase in near-normal angles. This implies that beaches where the coastline orientation changes substantially, e.g. due to km-scale nourishments, become potentially more dangerous to swimmers due to strong currents that develop with pronounced bar patterns.

Plain Language Summary

Surf zone sandbars front many sandy beaches worldwide. Their dynamics are crucial to the development of potentially hazardous rip currents and the movement of sand between sea and land. Breaking waves drive this sand movement, and may organise the sand into a remarkable alternation of shallow sandbars and seaward-directed rip channels along the beach. The mechanism driving this pattern formation is relatively well-understood at straight coasts, but it is unknown how this translates to strongly curved coasts. Recently, this has become of particular interest with the increasing volumes of sand placed at the coast for coastal management purposes. Such mega-nourishments may locally change an otherwise straight coastline into a strongly curved coastline. We used a numerical model to study the sandbars along a strongly curved coast, inspired by the km-scale Sand Engine nourishment. We found that the variable coastline orientation causes an alongshore variation in the angle of wave approach and resulting currents. Sandbars develop pronounced patterns and move landward where waves approach normal to the shoreline, whereas patterns remain absent where waves arrive at an angle. We also show that nourishment shape and wave climate are both crucial to the formation of sandbar patterns and associated hazardous rip currents.

1 Introduction

Sandbars, submerged ridges of sand parallel to the shoreline, often possess a pronounced alongshore variability in cross-shore position and depth (Sonu, 1973; Lippmann & Holman, 1989; Van Enckevort et al., 2004) that is related to the imposed wave energy, grain size and profile characteristics (Wright & Short, 1984; Calvete et al., 2007). These crescentic patterns are characterised by shallow landward protruding horns and deep seaward protruding bays with alongshore wavelengths of $O(100\text{ m})$ and cross-shore amplitudes of $O(10\text{ m})$ (Van Enckevort et al., 2004). Field observations show that crescentic patterns typically arise in a few days under low to moderately energetic conditions following a storm, and tend to disappear under high-energetic conditions (Wright & Short, 1984; Almar et al., 2010) or under oblique wave incidence (Price & Ruessink, 2011; Contardo & Symonds, 2015). In some cases they may, however, persist for months or longer (Van Enckevort & Ruessink, 2003). Pattern formation and destruction often coincides with overall onshore and offshore sandbar migration, respectively.

The mechanism behind crescentic pattern formation includes horizontal circulation cells in the flow field, which preferably develop under shore-normal or near-normal waves (e.g. Falqués et al., 2000; Calvete et al., 2005; Thiébot et al., 2012). Through a positive feedback between flow and morphology the characteristic crescentic patterning arises in the sandbar. Under increasing angles of incidence, circulation cells become skewed, growth rates decrease and wavelengths of the crescents increase (Calvete et al., 2005). In line with observations in the field, Thiébot et al. (2012) demonstrated with model simulations that crescentic patterns no longer arise when waves approach sufficiently oblique ($\theta > 11^\circ$ at their outer bar crest at $\sim$3.5 m depth, where θ is the wave incidence angle with the shore-normal) and the breaking-induced alongshore current starts to dominate over cell circulation. Besides, oblique waves have been observed to straighten sandbars with pre-exisiting crescentic patterns (Price & Ruessink, 2011; Price et al., 2013; Contardo & Symonds, 2015), whereof the underlying mechanism can be found in Garnier et al. (2013).

So far, the main focus has been on pattern formation under an alongshore uniform forcing. However, coasts that are concave, like embayed beaches, or convex, such as shoreline sandwaves and km-scale nourishments, impose an alongshore variation in forcing in the surf zone due to the refraction pattern over the curved depth contours (e.g. Castelle & Coco, 2012; Rutten et al., 2018). Similarly, offshore perturbations can create an alongshore variation in forcing (offshore bathymetric anomaly or offshore island; Castelle et al., 2012; Bryan et al., 2013) and accordingly, in bar behaviour. For example, the breaker height may vary alongshore, which was suggested by Short (1978) to generate an alongshore variation in sandbar characteristics. Also, the wave angle may vary alongshore, and enforce an alongshore difference in crescentic patterning. Such a relation between angle and patterning was found on a seasonal scale along the man-made curved coast of the Sand Engine, located at the roughly southwest-northeast oriented coastline of the Delfland coast in the Netherlands (Figure 1). Prolonged low-energetic north-northwestern waves in the spring-summer season (Rutten et al., 2018) initiated the formation of patterns only at the northern side of the Sand Engine. Under these conditions no patterns formed along the western side, where the waves were presumably much more oblique. In the autumn-winter season, patterning at the northern side was erased, whereas patterns developed at the western side under storms passing from southwest to north-northwest. Thus, patterns developed at the western side when actual shore-normal wave exposure was limited due to the varying angle. Castelle and Ruessink (2011) simulated the effect of a time-varying wave angle on crescentic patterns along a straight coast. Here, time-varying angles with low obliquity (θ<6°, at 10.6 m water depth) resulted in crescents that were less pronounced than under time-invariant forcing, and moreover initiated an alongshore migration of the crescents that stimulated splitting and merging of the crescents. Time-varying angles including higher obliquity (θ> 6°), for at least 1 day, resulted in straightening of crescents by a strong alongshore current. Notwithstanding, how a spatiotemporal variation in wave angle, as occurring along a curved coast, contributes to pattern formation and destruction is yet unknown.

We hypothesise that a spatiotemporal variation in the local wave angle enforces an alongshore variation in the presence and growth rate of crescentic patterns, depending on the strength of the alongshore current. In this paper, we aim to systematically explore how curvature of a convex coast contributes to alongshore variability in the formation of crescentic bar patterns under time-varying forcing. We use the non-linear morphodynamic model of Dubarbier et al. (2017), wherein cross-shore and alongshore processes are included such that an initially alongshore-uniform bar can move onshore and develop alongshore variabilities simultaneously. Although the model setup is loosely based on observations of pattern formation at the Sand Engine, we do not aim to mimic the crescentic bar behaviour at this site. First, we outline the model formulation, its setup and the analysis method of the model results (Section 2). Then, we describe the effect of the offshore wave angle on pattern formation (Section 3). In Section 4, we discuss the effect of variations in wave characteristics and coastline curvature. Finally, we conclude our findings in Section 5.

2 Methodology

2.1 Model

The formation of crescentic patterns in sandbars and their evolution was simulated with a non-linear morphodynamic model consisting of four coupled modules (Dubarbier et al., 2017). In the first module, the statistical wave field was computed by the spectral wave model SWAN (version 41.10 Booij et al., 1999), wherein we chose the dissipation formulation of Ruessink et al. (2003) and switched off local wave generation and the triplet and quadruplet wave-interaction source terms. In the second module, the 2D flow field was computed via the phase-averaged and depth-averaged non-linear shallow water equations, assuming balance of momentum and conservation of water mass, giving (Phillips, 1977):

$$\frac{\partial Q_i}{\partial t} + \frac{\partial}{\partial x_j}\left(\frac{Q_i Q_j}{h}\right) = -gh\frac{\partial \eta}{\partial x_i} - \frac{1}{\rho}\frac{\partial S_{ij}}{\partial x_j} + \frac{1}{\rho}\frac{\partial T_{ij}}{\partial x_j} - \frac{\tau_i^b}{\rho}, (i, j = 1, 2) \qquad (1)$$

$$\frac{\partial \eta}{\partial t} = -\frac{\partial Q_j}{\partial x_j} \qquad (2)$$

Using the Einstein convention, subscript i refers here to the two horizontal position coordinates (with X and Y the cross-shore an alongshore axis). This implies that terms containing an index twice include a summation over both indices. In these equations,

Q_i is the fluid volume transport, η is the mean free surface elevation, S_{ij} is the radiation stress tensor, T_{ij} is the lateral mixing term that describes the horizontal momentum exchange due to breaking-induced turbulence and the mean current, τ_i^b is bed shear stress, t is time, x is position, h is water depth, g is gravitational acceleration, and ρ =1000 kg/m^3 is water density. The wave return flow (undertow) was taken into account through the wave radiation stress formulation of Phillips (1977). In the third module, the total volumetric sediment transport $\vec{q_t}$ was computed with an energetics-type transport model composed of three modes of transport, based on Hsu et al. (2006) and Dubarbier et al. (2015), as

$$\vec{q_t} = \vec{q_w} + \vec{q_c} + \vec{q_g} \tag{3}$$

with a transport related to near-bed orbital velocity skewness $\vec{q_w}$, a transport related to the mean current $\vec{q_c}$, and a diffusion term $\vec{q_g}$ representing the downslope gravitational transport that prevents unrealistic bar growth and/or unstable bar shapes. More specifically, $\vec{q_w}$ accounts for wave non-linearity, but does not include infragravity or swash motions. Hereto, the intra-wave motion is reproduced using the robust parameterisation of Ruessink et al. (2012) that relates values of wave-skewness and asymmetry to the local Ursell number, all derived from field measurements of the statistical wave field and mean water level. The sediment transports $\vec{q_w}$, $\vec{q_c}$, and $\vec{q_g}$ contain both bedload and suspended load, with scaling coefficients of 0.135 and 0.015, respectively. The contribution of the three individual transport components to $\vec{q_t}$ is scaled with coefficients C_w, C_c, and C_g of 0.08, 0.08 and 0.24, respectively. For the specific definition of $\vec{q_w}$, $\vec{q_c}$, and $\vec{q_g}$, see Dubarbier et al. (2017). In the fourth module, bed level change was computed, assuming conservation of sediment mass, as

$$\frac{\partial z_b}{\partial t} = -\frac{1}{1-p}\vec{\nabla} \cdot \vec{q_t} \tag{4}$$

with bed level z_b and sediment porosity p =0.4.

By looping through the four modules, small perturbations in the bathymetry can grow and self-organise into rhythmic patterns through positive feedback between the bed level and the flow field. For further details on the model, see Dubarbier et al. (2017).

This model allows sandbars to develop crescentic patterns while moving onshore across the surfzone. The capability of the model to simulate cross-shore dynamics, besides alongshore dynamics, is important when investigating pattern formation along curved coasts, because alongshore variability in cross-shore migration may importantly affect pattern formation. For example, the separation distance of the bar from the shoreline is known to be critical to crescentic bar dynamics (Calvete et al., 2007). Simulating accurately cross-shore bar migration is a challenge by itself and therefore often comes to compromises. In this state-of-the-art model, cross-shore migration speed and direction of the bar, depending on the velocity field and sediment characteristics (Dubarbier et al., 2017), can be tuned by changing the ratio and magnitude of the transport coefficients. Furthermore, the model is able to properly simulate pattern formation under a wide range of local wave incidence, as observed along the curved coastline of the Sand Engine. Preliminary tests at a straight coast showed that crescentic patterns could develop under higher incidence angles using the nonlinear model of Dubarbier et al. (2017) than using a nonlinear model with the basic-state approach (e.g. Castelle et al., 2012; Garnier et al., 2008). Although linear stability models, also based on a basic state, may produce crescentic patterns under higher incidence angles as well (e.g. Ribas et al., 2011), such models do not include cross-shore bar migration and thus are not suitable for this study. Moreover, note that linear stability models are rather different from nonlinear models, and therefore results cannot be compared directly.

2.2 Model Setup

A synthetic bathymetry was created, based on *in situ* measurements of the Sand Engine in November 2014 (Figure 2). The synthetic bathymetry is a simplification of reality as the coastline does not show any asymmetry and the cross-shore profiles do not vary alongshore. First, a curved coastline was generated using a Gaussian shape function

$$X = p_1 + p_2 e^{-\frac{(Y+p_3)^2}{2p_4^2}} \tag{5}$$

with alongshore distance Y, cross-shore distance X, and function coefficients $p_1 = 253.36$ m, $p_2 = -698.37$ m, $p_3 = -494.33$ m, and $p_4 = -926.30$ m following from the best nonlinear fit through the measured 0 m contour line (Mean Sea Level, MSL). The alongshore axis was aligned with the regional coastline and the cross-shore axis pointed into the dunes (negative values offshore). Second, a barred cross-shore profile was generated using the double slope profile function of Yu and Slinn (2003)

$$z_{prof} = \left(x_s - \frac{x_s}{\gamma}\right)\tanh\left(\frac{\tan\beta_1 X}{x_s}\right) + \frac{\tan\beta_1 X}{\gamma} - b_h e^{-b_w\left(\frac{X-x_c}{x_c}\right)^2} \tag{6}$$

with bed elevation z_{prof}, and function coefficients $\gamma = \tan\beta_1/\tan\beta_2$, $\beta_1 = 0.0372$, $\beta_2 = 0.0112$, $x_s = 3.63$ m, $x_c = -222.6$ m, $b_h = -2.39$ m, and $b_w = 11.07$ m, which followed from the best non-linear fit with the measured alongshore-averaged profile (over a 500 m box) at the western side of the Sand Engine in November 2014. In Equation (6), the first term and second term on the right-hand side create a profile with slope β_1 in the upper part, changing at cross-shore position x_s into slope β_2 for the lower part of the profile. The last term creates a perturbation of amplitude b_h and width b_w at cross-shore position x_c, representing the sandbar. The profile extends up to +2 m MSL to anticipate for surged water levels. Third, the cross-shore profile was rotated along the Gaussian-shaped 0 m contour, resulting in a bathymetry with an alongshore-uniform subtidal bar located at equal distance from the curved shoreline. Fourth, the generated bathymetry was linearly interpolated on a Cartesian grid, as required by the model. The computational grid extended 2600 m in the cross-shore and 7000 m in the alongshore direction, with equal cross- and alongshore grid sizes of 10 m. Fifth, depths beyond −15 m MSL were replaced by −15 m, and the bathymetry between the −12 m contour and the offshore boundary was recomputed to create a gradual fading of the Gaussian-shaped perturbation in these deep contour lines (see Figure 2b). Finally, random perturbations of <0.01 m were added to the bathymetry to trigger pattern formation in the nearshore zone.

Additional bathymetries were created with larger, smaller or zero coastline curvature to test the curvature effect on alongshore differences in crescentic bar patterns. The three additional bathymetries differed from the reference bathymetry in the cross-shore extension of the coastline perturbation, i.e. $p_2 = -698.37$ m in Equation (5) was adjusted to $p_2 = -931.16$ m (initial extension of the Sand Engine, in 2011), $p_2 = -349.18$ m (half of the extension of the reference bathymetry), and $p_2 = 0$ m (straight coast).

The influence of the significant wave height H_s and a time-varying wave angle θ on nearshore pattern formation were tested by running the model with sets of scenarios, providing information for examining our hypothesis on the importance of a spatiotemporal variation in local wave angle along curved coasts. Scenarios were inspired by wave conditions prevailing during the observed formation of crescentic patterns in the sandbar at the western side of the Sand Engine. As shown by Rutten et al. (2017, 2018), patterns developed at this side in autumn and winter with the passage of one or several storms. During such storms, the wave angle typically changed from southwest to north-northwest, which can be attributed to the southwest-northeast oriented storm track in the North Sea. The forcing of every storm was slightly different, i.e. the dominant wave angles, the period and the function of the wave angle alternation as well as the wave height vary between the storms. To investigate how a series of storms with a time-varying angle may trigger pattern formation along a barred curved coast, various scenarios were generated whereof the wave conditions applied at the offshore boundary are summarised in Table 1. The storms were schematised as an alteration of the wave angle θ between two directions (θ_1 and θ_2), and consequently a series of storms was schematised by repeating the angle alternation several times. The ranges in θ, significant wave height H_s, and alternation period or function, covering the ranges in wave conditions observed at the Sand Engine (Rutten et al., 2017), allow to explore alongshore variability in crescentic pattern formation along curved coasts under time-varying forcing in a general sense. The most simple scenario (Ref_1), not including any time-varying forcing, has an offshore wave angle that is shore-normal at the left flank with $H_s = 2.0$ m and $T_p = 8.0$ s and is expected to generate patterns at the left flank. Sensitivity to the wave angle itself was tested by variations on the time-invariant angle with θ_1=θ_2 and $-55 \leq \theta_1 \leq 55°$ (Runs 1-11). The simplest scenario with a time-varying angle had a symmetric forcing, i.e. the wave angle alternating abruptly every day from shore-normal at the right flank ($\theta_1 = 25°$) to shore-normal at the left flank ($\theta_2 =-25°$) of the perturbation and served as reference, named Ref_2, for all time-varying scenarios throughout the article. Asymmetry in forcing and wave obliquity with respect to the flanks was tested in Runs 12-21, wherein θ_2 was fixed at $-25°$ and $-55 \leq \theta_1 \leq 55°$. Additional angle variations included the function of alternation (Runs 22-29) with gradual alternations from θ_1 to θ_2 following a cosine and sawtooth function, and the period of angle alternation with a duration Dur_1 and/or Dur_2 of 0.5, 1.5 and 2.0 days (Runs 30-35). Sensitivity to wave height was tested by varying $1.6 \leq H_{s,1} \leq 2.4$ m while keeping $H_{s,2}$ constant at 2.0 m (Runs 36-39). In all runs a directional spreading of 30° was used. This value, assumed as typical for the North Sea, resulted in offshore leakage of wave energy at the offshore boundary under large wave angles (up to 9.3% for 55°). Bathymetric variations (Runs 40-48) were applied to test the aforementioned effect of coastline curvature on pattern formation. On a strongly curved coast, a gently curved coast and a straight coast, three scenarios were tested that differed in θ_1, with $\theta_1 = 25°$ (Runs 40-42), $\theta_1 = -25°$ (Runs 43-45), and $\theta_1 = 55°$ (Runs 46-48).

In $\vec{q}_w$, $\vec{q}_c$, and $\vec{q}_g$ a median grain diameter d_{50} of 290 μm was used. Based on preliminary runs, scaling coefficients C_w, C_c and C_f, corresponding to the individual sediment transports, were adjusted from their default 0.08, 0.08, and 0.24 to 0.02, 0.04, and 0.05, respectively. This setting allowed a formation and evolution of crescentic bar patterns that resemble the field observations at the Sand Engine in Rutten et al. (2018), but with an over predicted onshore bar migration. Realistic cross-shore migration rates were not pretended for this work. Cross-shore dynamics were speeded up to limit the computation time of the 50 runs on a 2.6 km by 7 km grid. Speeding up the cross-shore migration, consequently speeded up cross-shore profile change (e.g. depth of bar crest or trough). Since crescentic bar dynamics (i.e. rip spacing and growth rate) were found to relate to profile shape (Calvete et al., 2007), biased bar migration predictions could affect those dynamics. At the Sand Engine, rip spacing hardly changed while the bars moved onshore and offshore at weekly to monthly timescales (Rutten et al., 2018). Also, Dubarbier et al. (2017) demonstrated that rip spacing and dynamics hardly changed during onshore bar migration under shore-normal wave incidence. Thus, the response time related to rip spacing seems to be larger than the response time related to cross-shore sandbar migration. Therefore we can speed up the onshore migration without harming the results on pattern formation.

Here, morphological change was simulated for a 20-day period, updating the bed level every 30 minutes. The 20-day period allows the growth rate of the patterns in the reference scenario to saturate. For each updated bathymetry, the corresponding wave field and flow field were computed in stationary mode. Periodic lateral boundaries conditions were used. In line with Castelle et al. (2012), the shoreline was allowed to evolve by computing the sediment fluxes at the cell centres and interpolate them at the cell interfaces. Accordingly, the sediment fluxes could transfer across the interface between dry and wet cells.

2.3 Analysis of Model Results

To reveal insight in the evolution of sandbar patterns and the underlying flow field, stacks of a time-varying transect were created along the alongshore-averaged bar crest position. The definition of the alongshore transect is not trivial. First, the model allows cross-shore sandbar migration, and thus the position of the alongshore transect needs to be updated every time step, following the cross-shore migration of the sandbar crest. Second, alongshore differences in cross-shore bar migration exist at a curved coast, and thus the alongshore-averaged profiles cannot simply be a global alongshore average but needs to be determined at a local scale. Here, we introduce a six-step approach to create time stacks along a curved coast. First, the bathymetry, z_b, was projected on local shore-normal transects, $z_{b,n}$, following the curved coastline. Shore-normal transects were directed perpendicular to the tangent of the 10 m depth contour in the bathymetry at $t = 0$ without including perturbations. Second, alongshore-averaged profiles, $\overline{z_{b,n}}$, were computed by applying a moving average to the cross-shore profiles over an alongshore width of ~500 m. Third, the second derivatives corresponding to the profiles, $d^2\overline{z_{b,n}}/dn^2$, were computed. Herein, smoothed profiles, using a 5-point Hanning window, were used, since the second derivative is rather sensitive to irregularities. Fourth, the bar crest positions were approximated by finding the minimum in $d^2\overline{z_{b,n}}/dn^2$ that was nearest to the bar crest of the previous time step. Fifth, the bar crest location was determined at subgrid scale to allow for gradual onshore migration of the alongshore transect instead of discrete steps of 10 m corresponding to the grid resolution. Hereto a second order polynomial was fitted through $d^2\overline{z_{b,n}}/dn^2$ at the bar crest approximation and its two neighbouring data points, giving a time-varying alongshore transect, $(X, Y)_t$. Sixth, bed elevation, the alongshore current and the total sediment transport, i.e. the variables of interest, were linearly interpolated along $(X, Y)_t$, and will be referred to as $z_{b,c}$, $U_{ls,c}$, and $\vec{q}_{t,c}$, respectively.

To analyse the growth rate of crescentic patterns, a measure was computed for the amplitude of the patterns on every time step. Previous studies (Garnier et al., 2006, 2010) computed the time-varying standard deviation of the bathymetry, a method known as global analysis. More specifically, they computed the root-mean-square deviation of the bathymetry from the time- and alongshore-averaged profile. Here, such a global approach is not sufficient, because the alongshore variability in pattern growth rate is of interest. Therefore, we performed calculations at a local scale, in sections at the left straight coast, the left flank, the right flank, and the right straight coast (boxes I-IV in Figure 2b). Preliminary analysis showed that onshore bar migration at a curved coast introduces an alongshore variability related to migrational dynamics that contaminates the time- and intersectional average of the cross-shore profile and thereby the measure for pattern amplitude. Therefore, each section was divided into two subsections of about equal size. Then, the measure for pattern amplitude in each section followed from the weighted average of the standard deviation in the two corresponding subsections, also known as the pooled standard deviation. In equation-form, this measure for pattern amplitude $||h||$ in a section reads as

$$||h|| = \sqrt{\frac{1}{N_1 + N_2 - 2}\left(\sum_{N_1} Z_{p,1}^2 + \sum_{N_2} Z_{p,2}^2\right)} \tag{7}$$

and increases with increasing potential energy density of the bedforms ($0.5||h||^2$, Vis-Star et al., 2008). N_1 and N_2 are the number of elements in subsections 1 and 2, respectively. The deviation from the alongshore-averaged profile in a subsection reads as $Z_p(N,t) = z_{b,n}(N,t) - \overline{z_{b,n}}(t)$, with N as the shore-normal transect. Herein, bed elevations interpolated at the shore-normal transects, $z_{b,n}$, were used.

The cross-shore and alongshore components of the flow vector field have often been found to be important variables to explain pattern formation (e.g. Garnier et al., 2013; Price et al., 2013). At a straight coast, the x- and y-component of a vector simply represent the cross-shore and alongshore component, respectively. Along a curved coast, however, the cross-shore and alongshore direction vary locally, and thus a local matrix rotation is needed to obtain a fair representation of both the cross- and alongshore component. The rotation angle ϕ in the rotation matrix was determined for every shore-normal transect. Then, the variable of interest, i.e. flow vector field, was linearly interpolated to shore-normal transects. Finally, the matrix rotation was applied to obtain the alongshore current U_{ls}. Similar to a vector field, a curved coast complicates interpretation of wave angles. The model gives the wave angle θ with respect to the global coastline orientation, while the wave angle with respect to the local coastline orientation may strongly differ along a curved coast. Here, the local wave angle θ_l was computed from the difference between the global wave angle θ and ϕ, where 0° denotes shore-normal incidence and positive values indicate waves coming from the right. The local breaker angle $\theta_{l,b}$

was defined as the local angle corresponding to the maximum wave height, hereafter referred to as the breaker wave height H_b, at a shore-normal transect.

3 Results

3.1 Reference Scenarios

To interpret the results of the full set of scenarios, we first examine two reference scenarios, with a time-invariant angle and a time-varying angle, respectively.

3.1.1 *Time-Invariant Angle* Ref_1

Figure 3 shows that the onshore migrating sandbar develops crescentic patterns along a large part of the coast. On $t = 19$ days, several crescents have formed along the left flank and the straight coast, while rhythmic morphology lacks along the right flank.

Figure 4a-c shows the significant wave height H_s, the total sediment transport $\vec{q}_t$, the bed level change rate Δz_b and the wave and current vectors at $t = 0$ days when the sandbar is still alongshore uniform. For the same day, Figure 5 shows, for each cross-shore profile, the wave height at breaking H_b, the local angle at breaking $\theta_{l,b}$, the alongshore current at the bar crest $U_{ls,c}$ and the total sediment transport at the bar crest $\vec{q}_{t,c}$. The abrupt cross-shore drop in H_s in Figure 4a, indicated by the change in colour shading (red to yellow), is caused by wave breaking at the bar crest. The alongshore variation in H_s and H_b can be explained by the refraction pattern. At the left flank (section II), waves propagate nearly normal to the depth contours and thus hardly refract, except for the waves traveling over the offshore part of the bathymetry (between 15 m and 12 m MSL the shape of the depth contours changes gradually from straight to curved, see Figure 2). The limited refraction results in limited divergence of the wave rays, limited redistribution of the wave energy, and thus a minor decrease in H_s and H_b. At the same time along the right flank (section III), waves approach the coast obliquely (angle of ∼-50°), and consequently their energy and height reduces substantially when propagating onshore due to strong refraction. Here, $\theta_{l,b}$ is still substantial (∼-24°). At the adjacent beaches (sections I and IV), where waves approach the coast under an angle of ∼-25°, refraction is limited and $\theta_{l,b}$ relatively small (∼-9°; Figure 5b). Note that H_b in Sections I and IV differs increasingly towards the flanks (compare $-2400<Y<-1600$ m with $2600<Y<3400$ m Figure 5a). Such secondary variations in H_b and H_s are again related to refraction, but now at a global scale, due to wave focussing caused by the alongshore variability in the depth contours. The concave shape in the contours at the right flank enhances the divergence of the wave rays and thus H_s and H_b decrease further (1500<Y<3500 m; Figure 4a and Figure 5a), while the convex shape causes the wave rays to converge and thus H_s and H_b increase substantially (around the tip). In contrast to the right side, wave divergence and the consequent reductions in H_s and H_b are hardly present near the concave shape at the left flank (Y =−1300 m) as the bending of the wave rays is limited under the low oblique waves here. Besides, H_s and H_b in Section I are slightly affected by the wave divergence in Section III and IV due to the periodic boundaries.

Figure 4c (blue arrows) and Figure 5c show that the alongshore current is of moderate strength (∼0.21 m/s) and rightward directed along the straight coast, nearly zero at the left flank, and strongest (∼0.5 m/s) at the right flank. In Section IV, the substantial differences in H_b are not reflected in $U_{ls,c}$ because of the inverse effect of $\theta_{l,b}$ on $U_{ls,c}$. In Section II, the near-zero alongshore current converges (downward zero-crossing in Figure 5c) and diverges (upward zero-crossing). At the convergence point, the opposing rightward and leftward directed alongshore current may have fed an offshore directed flow of small magnitude. The total sediment transport $\vec{q}_t$ (Figure 4b, red arrows) is of small magnitude and slightly onshore directed along the straight coast, almost absent at the left flank, and relatively large ($\vec{q}_{t,c}$ ∼6.2 x10^{-4} m^3/m/s; Figure 5d) and directed along the sandbar crest at the right flank. Although the pattern in $\vec{q}_t$ is largely in line with the flow vector field and thus dominated by sediment transport related to the mean-current ($\vec{q}_c$), also onshore directed sediment transport related to wave-skewness ($\vec{q}_w$) contributes to the total sediment transport and causes the cross-shore component of the total sediment transport to be zero (along right flank) or onshore directed (along straight coast and left flank).

Consequently, bed level change (Figure 4c), where erosion relates to positive gradients in the total sediment transport in the landward direction and deposition to negative gradients, results in a ∼30-40 m onshore bar migration along the entire coastline within the first four days. Thereafter, cross-shore migration starts to depend more strongly on the alongshore position. At the tip, the left flank and the straight coast onshore migration rates are about 6 m/day, while at the right flank only 2 m/day. Note that these migration rates are time-averaged and some temporal variation exists. For example, rates up to 9 m/day are found just left of the tip. While moving onshore, the bar steepens due to erosion at its seaward flank and deposition just shoreward of its crest (Figure 3) except for the right flank. Here the bar trough fills in and from $t = 12$ days onwards a terrace-shaped bar can be distinguished. Eventually, alongshore variability develops in the sandbar along the left flank and the straight coast (visible from $t = 10$ days onwards, Figure 3). More specifically, alongshore variabilities in the 2D horizontal flow field, i.e. onshore directed flow over shallower parts of the bar and seaward directed flow over the deeper parts, force the development of horizontal circulation cells, stimulating crescentic pattern formation through positive feedbacks. Note that the first rip channels ($Y = -600$ m and $Y = 600$ m) develop where the bar moved rapidly to shallower depths, letting patterns develop more easily through an increased cell circulation, and in absence of alongshore currents ($U_{ls,c} \sim 0$ m/s; Figure 5). Subsequently, patterns start to develop in Section IV ($t = 10$ days, Figure 3) and slightly later also in Section I. The small delay of Section I might be explained by a slightly higher $U_{ls,c}$ compared to Section IV. In Section II, the formation of a rip channel around $Y = -1100$ m may be partly stimulated by a small offshore directed flow, related to convergence of the alongshore current. However, this mechanism does not seem to have contributed substantially to pattern formation here, as patterns develop at nearly similar rate away from the convergence point in the flow field (e.g. sections I and II). The absence of crescents along the right flank of the perturbation can be explained by the strong alongshore-directed current (0.54 m/s) as the waves approach obliquely, hindering the development of cell circulation. The time evolution of the measure for pattern amplitude $||h||$ is shown in Figure 6 for four sections of the coast, revealing the alongshore variability in growth rate of the crescentic patterns. Initially, $||h||$ increases slowly. After $t = 5$ days, $||h||$ rapidly increases at the left flank (section II, blue line). At $t = 8$ days, $||h||$ starts also to increase for the sections with a straight coastline (sections I and IV; yellow and purple line). The growth rate slows down again at $t = 16$ days for the left flank (section II) and at $t = 18$ days at the right straight coast (section IV). At the right flank (section III), $||h||$ does not show a strong increase that is typical for pattern formation within the 20-day simulation period. Thus, $||h||$, estimated as pooled standard deviation, clearly describes the spatiotemporal variability in patterning as observed in Figure 3.

3.1.2 Time-Varying Angle Ref_2

By shifting θ at the offshore boundary, every day from 25° to −25°, the patterns in wave refraction, currents, sediment transport and bed level change are similar to the patterns described in Section 3.1.1 for $t = 0, 2, 4, ...18$ days but mirrored across the vertical in $Y = 500$ m for $t = 1, 3, 5, ...19$ days (e.g. black arrows in Figure 7). As a result, the sandbar migrates onshore and develops crescentic patterns along the straight coast but not along the flanks (Figure 7). Similar to Ref_1 the bar migrates by ∼35 m onshore in the first four days along the entire coastline, but only after t =12 days the migration rates start to show clear alongshore differences. At the straight coast and the tip rates increase up to 8 m/day compared to 2-3 m/day along the flanks. The lower rates at the flanks can be explained by a refraction-induced reduction of the wave height when the waves enter obliquely every other day at one of the flanks (wave divergence; Figure 5a). The strong alongshore current, leftward at the left flank (∼−0.5 m/s for $t = 0, 2, 4, ...18$ days; red line in Figure 5c) and rightward at the right flank (0.5 m/s; for $t = 1, 3, 5, ...19$ days; purple line in Figure 5c), may explain the absence of crescents here as they hinder the development of cell circulation. The first rip channels develop at the same location at the left and right straight coasts ($Y = -2280$ and $Y = 3250$ m). Figure 6b shows a slow increase in $||h||$ until $t = 8$ days, then $||h||$ increases rapidly for the sections with a straight coastline (sections I and IV; yellow and purple line). Compared to Ref_1, this increase starts slightly later for Section IV (purple) while slightly earlier for Section I (yellow). After $t = 18$ days, the growth rate becomes negative for Section I. Both flanks (Sections II and III; red and blue line) lack the typical strong increase in $||h||$ related to pattern formation within the 20-day simulation period. Thus Ref_2 shows that, in line with Ref_1, patterns preferably develop under low-obliquity (limited alongshore current and refraction-induced reduction of the wave height). Such conditions stimulate the bar to move onshore to shallower depths where patterns develop more easily. Under a time-varying wave angle, certain stretches of the coast may be subjected alternately to low and high obliquity. Ref_2 shows that low obliquity throughout the simulation period is important to develop patterns under a time-varying angle.

3.2 Effect of Wave Angle

Variations on both the time-invariant and time-varying angle (Runs 1-21; Table 1) show that alongshore variability in the presence of patterns change with the scenario.

Patterns arise where angles are low oblique throughout the simulation period and remain absent where angles are oblique for, at least, every other day. For the time-invariant angle scenarios, the position where patterns develop simply shifts with the imposed offshore wave angle (not shown). More specifically, hardly any pattern arises under -55° or 55° (Run 1, 11), but arise along the left flank (Section II) for -45 to -5° (Runs 2-5, Ref_1), along the straight coast (Sections I, IV) for -25 to 25° (Runs 4-8, Ref_1) and along the right flank (Section III) for 5-45° (Runs 6-10).

The interpretation of the time-varying angle scenarios (Runs 12-21) is less intuitive. Half of their simulation time the offshore angle equals -25°; in Ref_1 such an angle stimulated pattern formation along the left flank and the straight coast but prevented them to form along the right flank. During the other half of the time, the wave angle may be substantially different and thus stimulate or prevent pattern formation at entirely different positions. Figure 8 shows the bathymetries of the time-varying scenarios at $t =$ 19 days. Within all scenarios, not any pattern develops along the right flank (Section III), where waves approach rather obliquely every other day ($\theta_2 = -25°$, $\theta_{l,b} = -24°$). As long as the forcing is from the left side only (Runs 12-16), crescentic patterns develop along the left flank (section II). In the two-sided scenarios (Runs 17-21), no patterns develop here, except for Run 17 with $\theta_1 = 5°$. Scenarios with one- as well as two-sided conditions create patterns along the straight coast (sections I and IV) if $|\theta_1| \leq 35°$(Runs 15-19, Ref_1 and Ref_2). Figure 9 shows the temporal evolution of the depth in the bar zone for the different time-varying scenarios (first column), and illustrates that the growth rates of crescentic patterns vary strongly both within and between the scenarios (second column). The time period at which the growth of alongshore variability in depth and position of the bar crest stabilises varies from several days to beyond the simulation period of 20 days. Generally, crescentic patterns start to clearly develop within the simulation period where maximum $\theta_{l,b}$<13°, and they develop the fastest along stretches of the coast where wave obliquity is the smallest. For example, in Run 17 crescentic patterns develop first along the straight coast (sections I and IV), and subsequently start to form along the left flank (section II). This alongshore difference in growth rate can be clearly noted in the time evolution of $||h||$ corresponding to the four sections (Figure 9; Run 17). Here, waves approach rather obliquely half of the time ($t = 0, 2, ..., 18$ days) along the left flank ($\theta_{l,b}$~15°), whereas the straight coast is exposed to smaller obliquity ($\theta_{l,b}$~9° on $t = 1, 3, ..., 19$ days). This confirms the preference of crescentic patterning for low obliquity. Furthermore, Figure 9 shows that crescents along the straight coast (sections I and IV) migrated alongshore in rightward direction (rates up to ∼20 m/day) in Runs 14-15 and Ref_1 wherein waves approached from the left side only. Zooming in shows that crescents in Runs 18-21 and Ref_2 migrated alternately leftward and rightward, correlating with the alternating wave angle between the left side and right side.

In line with the reference scenarios, local obliquity may prevent or slow down the formation of crescentic patterns because of reduced local wave heights, and strong alongshore currents that inhibit cell circulation. The third column in Figure 9 shows the alongshore current $U_{ls,c}$ for the different time-varying scenarios on $t = 0$ days (blue line) and $t = 1$ days (red line), wherein positive and negative values indicate a rightward and leftward directed current, respectively. All one-sided scenarios (Runs 12-16) generate an alongshore current that is alternately small (condition 1: $t = 0, 2, ...18$ days) or near-zero (condition 2: $t = 1, 3, ...19$ days) along the left flank (section II). Presumably, horizontal cell-circulation prevails during the full 20-day simulation period (both condition 1 and 2), stimulating crescentic pattern formation within this section. At the same time, large continuously rightward directed $U_{ls,c}$ along the right flank (section III) prevents circulation cells and crescentic patterns to develop here. In Runs 19-21 both the flanks and the straight coast are subjected to large incidence angles (under either θ_1 or θ_2), and thus large $U_{ls,c}$, inhibiting formation of distinct alongshore variability. Along the straight coast (sections I and IV), increased crescentic growth rates towards Runs 16-17 can be explained by the increase in shore-normal waves during condition 1 (θ_1), and thus decrease in the magnitude of $U_{ls,c}$. Similarly, the fastest growth rate of crescentic patterns along the left flank (section II) can be observed in Ref_1, when $U_{ls,c}$ ∼0 under both θ_1 and θ_2. Near-normal waves stimulate the development of crescentic patterns also because wave energy barely redistributes due to refraction, resulting in a relatively high H_b and consequently strong cell circulation. In addition, an offshore directed current related to convergence of the alongshore current may have stimulated rip channel formation at the convergence point (downward zero-crossing in right column of Figure 9). This mechanism becomes more important for runs with a stronger alongshore current around the convergence point and thus a stronger offshore directed current. Run 16 crashed at $t = 10.9$ days, possibly due to the fast onshore bar migration near the tip of the curved coast, which resulted in a flow field too complex to be solved by the model. The results of Run 16 that are included above were obtained by performing the simulation with a smaller morphological time step of 15 minutes, which prevented crashing.

The importance of low obliquity on the alongshore variability in presence and growth rates of crescentic patterns is corroborated by simulations with gradually varying θ, following either a sawtooth curve (Runs 22-25) or a cosine function (Runs 26-29). Figure 10 shows that $||h||$ increases more rapidly at the straight coast (sections I and IV) for both sawtooth (dotted line) and cosine variations (dashed line). For example, $||h||$ in section I increases beyond 0.05 m after 7.2 days in Run 22 (sawtooth) and after 7.9 days in Run 26 (cosine), while it takes 10.6 days in Run Ref_2 having the same θ_1 and θ_2 but with an abrupt alternation. In addition, the sawtooth variations give a relatively large $||h||$ for the right flank (section III, red dotted lines in Figure 10), which related to the cascading of patterns in section IV into section III. Higher $||h||$ can be explained by the locally increased exposure time of near-normal waves, especially in the sawtooth variations, and thus shorter exposure to large $U_{ls,c}$ under a gradually varying θ. Although Run 23 crashed at $t = 17.4$ days and Run 27 at $t = 18.7$ days, the trends in $||h||$ are clear. Therefore, no additional simulations were run to cover the full 20-day period. The influence of exposure to low obliquity on the pattern formation is additionally reflected in Runs 30-32, indicating that longer exposure (up to 2 days) of shore-normal waves at the right flank results in increased growth rates (not shown). The chronology in the time-varying forcing has no substantial effect on pattern formation for exposure times between 0.5 day (Run 33) and 2 days (Run 35; not shown).

To summarise, the overall picture that arises from our simulations is that alongshore variability in the presence of crescentic patterns and their growth rate at a curved coast vary with the local wave angle. Low obliquity stimulates pattern formation through increased cell circulation because of a limited alongshore current and limited refraction-induced energy reduction (and thus high H_b).

4 Discussion

4.1 Comparison with Observations and Model Limitations

To show that the processes important to crescentic pattern formation are well included in the model, two comparisons are made with observations at the Sand Engine nourishment. Note that reaching exact quantitative agreement is beyond the scope of both our model and study aim, and that such agreement has not been reached with any other morphodynamic model applied to barred coasts under complex wave conditions.

Firstly, we analyse pattern formation under a time-invariant wave angle, comparing Run 8 with a 12-day period of north-northwestern waves with similar properties ($\overline{H_s}$=1.0 m, $\overline{T_p}$=6.3 s, $\overline{\theta}$=332°; 1-12 March 2013) at the Sand Engine (Figure 11a-b). In both the predictions and observations, waves approached the right flank of the curved coast shore-normally. Distinct patterns developed within 14 days in the simulations and within 12 days at the Sand Engine. Patterns were found at the right flank and along the straight coast, while they remained absent at the left flank within both (Figure 11a-b). Before being exposed to the 12-day period of north-northwestern waves, hardly any pattern existed at the right flank but whether patterns existed at the straight coast is not clear from the available video images. The alongshore wavelength of the crescents were well predicted at the straight coast (∼450 m), but over predicted at the right flank (450 m versus 300 m; Figure 11a-b). The largest differences between predictions and observations are found in the cross-shore dynamics. The simulated bar, initially located at ∼230 m from the 0 m contour at 2.6 m depth, migrated onshore with ∼7 m/day over 16 days. The observed bar was located only ∼120 m from the 0 m contour with its crest at 2.3 m depth and migrated 18 m onshore within the 12-day period of pattern formation.

Secondly, we analyse pattern formation under a time-varying angle. At the Sand Engine, patterns developed at the left flank within a 17-day period ($\overline{H_s}$=1.3 m, $\overline{T_p}$=6.0 s, $\overline{\theta}$=293°; 2-19 November 2013) wherein several storms passed by with an angle that changed within ∼2 days from west to west-northwest, from west to northwest or from west-northwest to northwest, depending on the storm. Because of the variety in storms, we compare the observations with two runs, having an angle that switched abruptly after a day between either -55 and -25° (Run 12) or -25 and 5° (Run 17). In the observations, patterns developed within 17 days at the left flank and the straight coast. Some minor alongshore variability arose at the right flank after 9 days. In Run 12 only some patterns developed at the left flank after 16 days, but in Run 17 patterns developed at both the left flank and the straight coast within 18 days (see Figure 8 and Figure 11c-d). The alongshore wavelength of the simulated crescents (Run 12: ∼500 m; Run 17: ∼440 m) compare well with the observations (on average ∼510 m; Figure 11). Alongshore migration rates are limited in both the predictions and the observations. Alike the time-invariant simulation, the largest differences are found in the cross-shore dynamics. The bar migrated onshore with ∼7 m/day in both runs, whereas a 3 m offshore migration was observed at the Sand Engine. The shoreline at the Sand Engine retreated with 18 m, whereas the shoreline kept its position in the runs. After the patterns developed, the longshore-averaged bar crest depth in the runs was very similar to the observed one (2.2 m versus 2.3 m).

The differences in the simulated and observed onshore bar migration relate largely to the choice of the model coefficients. The relatively large coefficient for the wave-induced sediment transport (C_w) led, as intended, to an over predicted onshore migration speed of the bar and a speeding up of the computation time. Besides, some uncertainty exists in our observations of bar migration. The bar may have migrated further onshore than we observed, since the expected migration magnitude falls within the $O(10$ m$)$ accuracy of the breaker line method used by Rutten et al. (2018). Especially migration under the passage of storms (November 2013) may not have been well captured by the method, as variations in wave height can affect the position of the breaker line (Van Enckevort & Ruessink, 2001; Ribas et al., 2010). In addition, the observed shoreline position, used to compute the bar-shore distance in Figure 11, is only accurate up to $O(10$ m$)$ (Rutten et al., 2018).

Furthermore, some of the differences between the simulated and observed bed evolution can be explained by the prescribed boundary conditions in the model. First, we use a rather high wave period and wave height. Assuming that the storms drive the most important morphologic change, we included only those in our scenarios without any calm period as observed in the field. Consequently, the wave height and wave period in the scenarios is higher than the time-averaged forcing during pattern formation at the Sand Engine. Although considering storm forcing only, the wave period is still relatively high for the North Sea. However, when using a smaller value no patterns developed. Earlier, Calvete et al. (2005) found with a morphodynamic stability model that pattern growth rate decreases substantially with decreasing wave period, especially for oblique waves (see their Figure 15). Second, we schematised the time-varying angle as an alternation between two angles; a simplification that allowed to systematically explore its effects on pattern formation. However, measurements at the Sand Engine show more complexity, in terms of the angle itself as well as the alternation function. At times, the angle alternates between three angles. The angle alternation function varies over time, sometimes better resembling a sawtooth and sometimes a cosine or abrupt function. In addition, the simplifications made when defining the synthetic bathymetry may have led to important differences between the simulations and observations. We assumed an alongshore uniform profile, and thus without any variation in bar crest depth, bar height, bar width, bar position or shoreface slope. At the Sand Engine, some differences in profile existed between the left flank and the right flank (Rutten et al., 2018) and pattern formation events never started without any patterns somewhere along the coast. To illustrate this, the over prediction of the crescent wavelength at the right flank under a time-invariant angle may partly be related to such differences in the initial profile. Also, differences in bar behaviour at the straight coast adjacent to the right flank probably relate partly to the presence of a channel that connects the sea with the shallow lagoon at the Sand Engine (see Figure 2a) and wherein the flow reverses with every tide. Lastly, tides were neglected in our model setup. Morphologic change in the surf zone could be influenced by tide-induced water level variations (Price et al., 2013), tide-driven currents, but also other tide-induced phenomena specific for curved coasts (e.g. tidal flow separation, Radermacher et al., 2017).

To summarise, the model can capture the formation of patterns with the right orders of magnitude (e.g. alongshore wavelength of crescents, pattern growth rate), despite some model limitations. The patterns produced under a time-varying angle do not always develop where they were observed at the Sand Engine, given that the used wave schematisation deviates from the observed wave conditions. For observed nearly-constant wave angles, the location is accurately reproduced by the model.

4.2 Effect of Time-Varying Wave Height

How alongshore differences in patterning are related to the local wave angle was investigated above for a time-invariant wave height of 2.0 m. At the Sand Engine, the offshore wave height varied during pattern formation (Rutten et al., 2017, 2018). Here, we describe how our results on the formation of crescentic patterns are affected by a time-varying wave height (Runs 36-39, Ref_2; Figure 12). Generally, an increase in the wave height results in increased growth rates, consistent with Calvete et al. (2005) and Castelle and Ruessink (2011). Figure 12 also shows that a time-varying H_s affects the pattern growth rate differently within the four sections. The alongshore variability in presence or absence of patterns, however, is not substantially affected, as patterns start to develop along the straight coast (sections I and IV, yellow and purple line in Figure 12) and slowly extend along the flanks (sections II and III, blue and red line in Figure 12) within all runs.

To summarise, a time-varying wave height influences the pattern growth rate and its alongshore variability, but to a relatively small extent in comparison to a time-varying wave angle (compare Figure 9 and 12).

4.3 Variations on Coastline Curvature

Runs 1-39 illustrate that a curved coast imposes alongshore differences in the local wave angle, the resulting flow field, and consequently pattern formation. Below, we discuss how variations on the curvature of the coastline (Runs 40-48) affect pattern formation, which is relevant in the design of km-scale nourishments and the anticipated alongshore diffusion of such coastline perturbations in perspective of swimmer safety (e.g. km-scale nourishments can modify the large-scale flow pattern and generate km-scale tidal eddies, Radermacher et al., 2017). In fact, the coastline curvature is expected to affect crescentic pattern formation in a similar way as the offshore wave angle (i.e. influencing the alongshore variability in presence and growth rate), since for both sets of scenarios the local wave angles change as they are a function of the offshore wave angle and the coastline orientation. Here, we study the contribution of curvature on pattern formation under three wave climates only, whereof found in Section 3.2 to either create patterns along the straight coast (Run Ref_2: $\theta_1 = 25°$ and $\theta_2 = -25°$) but not along the flanks, to create patterns along the left flank but not along the right flank (Run Ref_1: $\theta_1 = \theta_2 = -25°$) or to create no patterns at all (Run 21: $\theta_1 = 55°$ and $\theta_2 = -25°$). Figure 13 shows that alongshore variability in the presence of crescentic patterns does not change substantially for the selected range of coastline curvatures, in contrast to the growth rate of $||h||$. In Runs 40-48 the growth rate decreases for a smaller curvature, in particular for the straight coast scenarios (Runs 42 and 45). The decrease in growth rate in sections I and IV (Runs 40-42) relates to an increasing magnitude of $U_{ls,c}$ with decreasing coastline curvature, from a range of 0.15-0.22 m/s at the strongly curved coast (Run 40) to 0.24 m/s (Run 42) at the straight coast in these sections. Note that the range values are based on the condition with the largest $U_{ls,c}$. The increase in $U_{ls,c}$ and resulting decrease in growth rate cannot simply be explained by the difference between the offshore wave angle and the coastline orientation, since they both do not change within sections I and IV. However, H_s reduces at the lee side of the curved coast (changing from left to right every day) due to divergence of the wave rays. This refraction-induced reduction in the wave height increases for coasts with stronger curvature, resulting in lower

$\theta_{l,b}$, H_b, and thus lower $U_{ls,c}$. In section II, the growth rate variation between Runs 43-45 also relates to $U_{ls,c}$, which varies from 0.003-0.13 m/s (Ref_1) to 0.25 m/s (Run 45). Here, the varying magnitude of $U_{ls,c}$ depends mainly on the coastline orientation in section II. Besides, the left flank in these runs is not as strongly subjected to refraction as in Runs 40-42 since waves do not approach as strongly obliquely here. In Figure 13, information of Run 43 is partly missing, because the run crashed at $t = 10.7$ days. Attempts to simulate the full 20-day period using a smaller morphological time step of 15 or 10 minutes were unsuccessful. No patterns arise within the 20-day simulation period in Runs 46-48, which can be explained by the relatively large $U_{ls,c}$ of 0.15-0.57 m/s along the entire coastline under either θ_1 or θ_2, irrespective of a curved coastline.

Overall, our simulations demonstrate that rip channels, located between the lunate-shaped shoals of the crescentic bar, may develop at faster rate and become deeper with increasing curvature of the coastline, if the latter produces an increase of the percentage of near-normal local incidence. Under a time-invariant and a time-varying wave climate with limited obliquity, we found that curved coasts impact rip channel dynamics along their flanks as well as their adjacent straight coastlines because of the alongshore varying coastline orientation and the global refraction pattern. Increased rip channel presence at the straight coasts adjacent to the curved coast can enforce localised beach and dune erosion (Thornton et al., 2007). Moreover, rip channels are associated with narrow and approximately offshore-directed flows (rip currents) which are the leading deadly hazard to recreational beach users worldwide (Castelle et al., 2016). Accordingly, both the design and location of km-scale nourishments must be carefully examined in perspective of the prevailing wave climate and the primary beach entries at the foreseen site.

4.4 Offshore Bar Migration and Straightening

A straightening and/or offshore migration of the bar, observed in the field (e.g. Lippmann & Holman, 1990; Gallagher et al., 1998; Holman et al., 2006; Price & Ruessink, 2011; Contardo & Symonds, 2015; Rutten et al., 2018), was roughly explored by running the model with a larger wave height, period or angle but without success. Running the model with another ratio of the transport coefficients probably allows such bar behaviour. Dubarbier et al. (2017) explored the parameter space of the transport coefficients for a bar-beach system based on the Gold Coast (Australia) and found that the migration direction depends on the ratio of C_w and C_c. Using the same model, Bouvier et al. (2019)

simulated an offshore migration at Sète beach, defining the ratio C_w:C_c an order of magnitude lower than in our work. To find a ratio that allows an offshore migration or a straightening of the bar at our site, the parameter space needs to be studied in more detail but this is beyond the scope of this article.

5 Conclusion

The formation of crescentic patterns was numerically simulated for an initially alongshore-uniform sandbar along a curved coast under a time-invariant and time-varying wave angle θ. We found that the presence and growth rate of patterns varied alongshore with the local breaker angle, $\theta_{l,b}$. Patterns arose within the 20-day simulation period where local obliquity was limited to $\theta_{l,b}$ <13°. Variations of θ, i.e. its value and the shape or period of its time-varying function, affected $\theta_{l,b}$ and thereby the alongshore variability in presence of patterns and their growth rate. The preference of low obliquity for crescentic pattern formation can be attributed to the limited strength of alongshore currents and limited refraction-induced wave height reduction. Both positively affect the generation of horizontal circulation cells in the flow field that initiate crescentic pattern formation through positive feedbacks between the flow field and the bed. Simulations in which the coastline curvature was varied, from strongly curved to straight, confirm the important negative effect of the alongshore current on pattern formation. The presence and growth rate of crescentic bar patterns and associated rip channels increased with coastline curvature, if the percentage of locally near-normal incidence increased as well (e.g. wave climate with low obliquity). Consequently, km-scale nourishments with a curved coast may enforce rip dynamics and associated flows that threaten swimmer safety.

Acknowledgments

J.R. and B.G.R. were supported by the Dutch Technology Foundation STW that is part of the Dutch Organisation for Scientific Research (NWO), and which is partly funded by the Ministry of Economic Affairs, under contract 12686 (Nature Coast: S1 Coastal Safety). T.D.P. was funded by the Dutch Organisation for Scientific Research (NWO), under contract 016.Veni.171.101. B.D. and B.C. were funded through projects CHIPO (ANR-14-ASTR-0004-01) and SONO (ANR-17-CE01-0014), respectively, from Agence National de la Recherche (ANR). J.R. acknowledges Alec Torres-Freyermuth for the financial support (CONACYT Project CB 2016/284430) during the review process of the article. Computer time for this study was provided by the computing facilities MCIA (Mésocentre de Calcul Intensif Aquitain) of the University of Bordeaux and the University of Pau and Pays de l'Adour. Field data used to create the synthetic bathymetry are from Rutten et al. (2018). Model output is available from Rutten et al. (2019).

References

Almar, R., Castelle, B., Ruessink, B. G., Sénéchal, N., Bonneton, P., & Marieu, V. (2010). Two- and three-dimensional double-sandbar system behaviour under intense wave forcing and a meso-macro tidal range. *Continental Shelf Research*, *30*(7), 781–792.

Booij, N., Ris, R. C., & Holthuijsen, L. H. (1999). A third-generation wave model for coastal regions 1 . Model description and validation. *Journal of Geophysical Research*, *104*(C4), 7649–7666.

Bouvier, C., Castelle, B., & Balouin, Y. (2019). Modeling the impact of the implementation of a submerged structure on surf zone sandbar dynamics. *Journal of Marine Science and Engineering*, *7*(117). doi: 10.3390/jmse7040117.

Bryan, K. R., Foster, R., & MacDonald, I. (2013). Beach rotation at two adjacent headland-enclosed beaches. *Journal of Coastal Research*, *SI 65*, 2095–2100.

Calvete, D., Coco, G., Falqués, A., & Dodd, N. (2007). (Un)predictability in rip channel systems. *Geophysical Research Letters*, *34*(L05605). doi: 10.1029/2006GL028162.

Calvete, D., Dodd, N., Falqués, A., & van Leeuwen, S. M. (2005). Morphological development of rip channel systems: Normal and near-normal wave incidence. *Journal of Geophysical Research: Oceans*, *110*(C10006). doi: 10.1029/2004JC002803.

Castelle, B., & Coco, G. (2012). The morphodynamics of rip channels on embayed beaches. *Continental Shelf Research*, *43*, 10–23.

Castelle, B., Marieu, V., Coco, G., Bonneton, P., Bruneau, N., & Ruessink, B. G. (2012). On the impact of an offshore bathymetric anomaly on surf zone rip channels. *Journal of Geophysical Research: Earth Surface*, *117*(F01038). doi: 10.1029/2011JF002141.

Castelle, B., & Ruessink, B. G. (2011). Modeling formation and subsequent nonlinear evolution of rip channels : Time - varying versus time - invariant wave forcing. *Journal of Geophysical Research*, *116*(F04008). doi: 10.1029/2011JF001997.

Castelle, B., Scott, T., Brander, R. W., & McCarroll, R. J. (2016). Rip current types, circulation and hazard. *Earth-Science Reviews*, *163*, 1–21.

Contardo, S., & Symonds, G. (2015). Sandbar straightening under wind-sea and swell forcing. *Marine Geology*, *368*, 25–41.

Dubarbier, B., Castelle, B., Marieu, V., & Ruessink, B. G. (2015). Process-based modeling of cross-shore sandbar behavior. *Coastal Engineering*, *95*, 35–50.

Dubarbier, B., Castelle, B., Ruessink, B. G., & Marieu, V. (2017). Mechanisms controlling the complete accretionary beach state sequence. *Geophysical Research Letters*, *44*, 5645–5654.

Falqués, A., Coco, G., & Huntley, D. A. (2000). A mechanism for the generation of wave-driven rythmic patterns in the surf zone. *Journal of Geophysical Research*, *105*(C10), 24071–24087.

Gallagher, E. L., Elgar, S., & Guza, R. T. (1998). Observations of sand bar evolution on a natural beach. *Journal of Geophysical Research*, *103*, 3203–3215.

Garnier, R., Calvete, D., Falques, A., & Caballeria, M. (2006). Generation and nonlinear evolution of shore oblique / transverse sand bars. *Journal of Fluid Mechanics*, *567*(2006), 327–360.

Garnier, R., Calvete, D., Falqués, A., & Dodd, N. (2008). Modelling the formation and the long-term behavior of rip channel systems from the deformation of a longshore bar. *Journal of Geophysical Research*, *113*(C07053). doi: 10.1029/2007JC004632.

Garnier, R., Dodd, N., Falqués, A., & Calvete, D. (2010). Mechanisms controlling crescentic bar amplitude. *Journal of Geophysical Research*, *115*(F02007). doi: 10.1029/2009JF001407.

Garnier, R., Falqués, A., Calvete, D., Thiébot, J., & Ribas, F. (2013). A mechanism for sandbar straightening by oblique wave incidence. *Geophysical Research Letters*, *40*, 2726–2730.

Holman, R. A., Symonds, G., Thornton, E. B., & Ranasinghe, R. (2006). Rip spacing and persistence on an embayed beach. *Journal of Geophysical Research: Oceans*, *111*. doi: 10.1029/2005JC002965.

Hsu, T.-j., Elgar, S., & Guza, R. T. (2006). Wave-induced sediment transport and onshore sandbar migration. *Coastal Engineering*, *53*, 817–824.

Lippmann, T. C., & Holman, R. A. (1989). Quantification of sand bar morphology: A video technique based on wave dissipation. *Journal of Geophysical Research*, *94*(C1), 995–1011.

Lippmann, T. C., & Holman, R. A. (1990). Quantification of sand bar morphology: A video technique based on wave dissipation. *Journal of Geophysical Research*, *95*, 11575–11590.

Phillips, O. M. (1977). *The dynamics of the upper ocean.* Cambridge: Cambridge University Press.

Price, T. D., Castelle, B., Ranasinghe, R., & Ruessink, B. G. (2013). Coupled sandbar patterns and obliquely incident waves. *Journal of Geophysical Research: Earth Surface*, *118*(3), 1677–1692.

Price, T. D., & Ruessink, B. G. (2011). State dynamics of a double sandbar system. *Continental Shelf Research*, *31*, 659–674.

Radermacher, M., Schipper, M. A. D., Swinkels, C., Macmahan, J. H., & Reniers, A. J. H. M. (2017). Tidal flow separation at protruding beach nourishments. *Journal of Geophysical Research: Oceans*, *122*. doi: 10.1002/2016JC011942.

Ribas, F., Ojeda, E., Price, T. D., & Guillén, J. (2010). Assessing the suitability of video imaging for studying the dynamics of nearshore sandbars in tideless beaches. *IEEE Transactions on Geoscience and Remote Sensing*, *48*, 2482–2497.

Ribas, F., De Swart, H. E., Calvete, D., & Falqués, A. (2011). Modeling waves, currents and sandbars on natural beaches: The effect of surface rollers. *Journal of Marine Systems*, *88*, 90–101.

Ruessink, B. G., Ramaekers, G., & Van Rijn, L. C. (2012). On the parameterization of the free-stream non-linear wave orbital motion in nearshore morphodynamic models. *Coastal Engineering*, *65*, 56–63.

Ruessink, B. G., Walstra, D. J., & Southgate, H. N. (2003). Calibration and verification of a parametric wave model on barred beaches. *Coastal Engineering*, *48*(3), 139–149.

Rutten, J., Dubarbier, B., Price, T. D., Castelle, B., & Ruessink, B. G. (2017). Crescentic bar patterns along curved coasts: observations and modelling. In *Proceedings coastal dynamics 2017* (pp. 1832–1842).

Rutten, J., Dubarbier, B., Price, T. D., Ruessink, B. G., & Castelle, B. (2019). Model output: Crescentic sandbar behaviour along a curved coast. doi: 10.5281/zenodo.2566497.

Rutten, J., Ruessink, B. G., & Price, T. D. (2018). Observations on sandbar behaviour along a man-made curved coast. *Earth Surface Processes and Landforms*, *43*, 134–149.

Short, A. D. (1978). Wave power and beach stages: a global model. In *Proceedings coastal engineering* (pp. 1145–1162).

Sonu, C. J. (1973). Three-dimensional beach changes. *The Journal of Geology*, *81*, 42–64.

Stive, M. J. F., De Schipper, M. A., Luijendijk, A. P., Aarninkhof, S. G. J., Van Gelder-Maas, C., Van Thiel de Vries, J. S. M., ... Ranasinghe, R. (2013). A New Alternative to Saving Our Beaches from Sea-Level Rise: The Sand Engine. *Journal of Coastal Research*, *290*, 1001–1008.

Thiébot, J., Idier, D., Garnier, R., Falqués, A., & Ruessink, B. G. (2012). The influence of wave direction on the morphological response of a double sandbar system. *Continental Shelf Research*, *32*, 71–85.

Thornton, E. B., MacMahan, J., & Sallenger, A. H. J. (2007). Rip currents, mega-cusps, and eroding dunes. *Marine Geology*, *240*, 151–167.

Van Enckevort, I. M. J., & Ruessink, B. G. (2001). Effect of hydrodynamics and bathymetry on video estimates of nearshore sandbar position. *Journal of Geophysical Research*, *106*, 16969–16979.

Van Enckevort, I. M. J., & Ruessink, B. G. (2003). Video observations of nearshore bar behaviour. Part 2: alongshore non-uniform variability. *Continental Shelf Research*, *23*(5), 513–532.

Van Enckevort, I. M. J., Ruessink, B. G., Coco, G., Suzuki, K., Turner, I. L., Plant, N. G., & Holman, R. A. (2004). Observations of nearshore crescentic sandbars. *Journal of Geophysical Research: Oceans*, *109*(C6). doi: 10.1029/2003JC002214.

Vis-Star, N. C., De Swart, H. E., & Calvete, D. (2008). Patch behaviour and predictability properties of modelled finite-amplitude sand ridges on the inner shelf. *Nonlinear Processes in Geophysics*, *15*(6), 943–955.

Wright, L. D., & Short, A. D. (1984). Morphodynamic variability of surf zones and beaches: a synthesis. *Marine Geology*, *56*, 93–118.

Yu, J., & Slinn, D. N. (2003). Effects of wave-current interaction on rip currents. *Journal of Geophysical Research*, *108*(C3). doi: 10.1029/2001JC001105.

Table 1. Overview of the runs. In reference run Ref_1 time-invariant wave conditions were simulated for a total duration of 20 days, while in Ref_2 a bimodal wave field was simulated by alternating the angle θ abruptly every day from θ_1 to θ_2. Variations on Ref_1 and Ref_2 include the forcing (Runs 1-39) and bathymetry (Runs 40-48). Red colours indicate the differences with Ref_2.

Run name	$H_{s,1}$	$T_{p,1}$	θ_1	Dur_1	$H_{s,2}$	$T_{p,2}$	θ_2	Dur_2	Other
Ref1	**2.0 m**	**8.0 s**	**25°**	**1 day**	**2.0 m**	**8.0 s**	**25°**	**1 day**	
Ref2	**2.0 m**	**8.0 s**	**25°**	**1 day**	**2.0 m**	**8.0 s**	**-25°**	**1 day**	
1	2.0 m	8.0 s	**-55°**	1 day	2.0 m	8.0 s	**-55°**	1 day	
2	2.0 m	8.0 s	**-45°**	1 day	2.0 m	8.0 s	**-45°**	1 day	
3	2.0 m	8.0 s	**-35°**	1 day	2.0 m	8.0 s	**-35°**	1 day	
4	2.0 m	8.0 s	**-15°**	1 day	2.0 m	8.0 s	**-15°**	1 day	
5	2.0 m	8.0 s	**-5°**	1 day	2.0 m	8.0 s	**-5°**	1 day	
6	2.0 m	8.0 s	**5°**	1 day	2.0 m	8.0 s	**5°**	1 day	
7	2.0 m	8.0 s	**15°**	1 day	2.0 m	8.0 s	**15°**	1 day	
8	2.0 m	8.0 s	**25°**	1 day	2.0 m	8.0 s	**25°**	1 day	
9	2.0 m	8.0 s	**35°**	1 day	2.0 m	8.0 s	**35°**	1 day	
10	2.0 m	8.0 s	**45°**	1 day	2.0 m	8.0 s	**45°**	1 day	
11	2.0 m	8.0 s	**55°**	1 day	2.0 m	8.0 s	**55°**	1 day	
12	2.0 m	8.0 s	**-55°**	1 day	2.0 m	8.0 s	-25°	1 day	
13	2.0 m	8.0 s	**-45°**	1 day	2.0 m	8.0 s	-25°	1 day	
14	2.0 m	8.0 s	**-35°**	1 day	2.0 m	8.0 s	-25°	1 day	
15	2.0 m	8.0 s	**-15°**	1 day	2.0 m	8.0 s	-25°	1 day	
16	2.0 m	8.0 s	**-5°**	1 day	2.0 m	8.0 s	-25°	1 day	
17	2.0 m	8.0 s	**5°**	1 day	2.0 m	8.0 s	-25°	1 day	
18	2.0 m	8.0 s	**15°**	1 day	2.0 m	8.0 s	-25°	1 day	
19	2.0 m	8.0 s	**35°**	1 day	2.0 m	8.0 s	-25°	1 day	
20	2.0 m	8.0 s	**45°**	1 day	2.0 m	8.0 s	-25°	1 day	
21	2.0 m	8.0 s	**55°**	1 day	2.0 m	8.0 s	-25°	1 day	
22	2.0 m	8.0 s	**25°**	1 day	2.0 m	8.0 s	-25°	1 day	**θ varies with sawtooth**
23	2.0 m	8.0 s	**35°**	1 day	2.0 m	8.0 s	-25°	1 day	**θ varies with sawtooth**
24	2.0 m	8.0 s	**45°**	1 day	2.0 m	8.0 s	-25°	1 day	**θ varies with sawtooth**
25	2.0 m	8.0 s	**55°**	1 day	2.0 m	8.0 s	-25°	1 day	**θ varies with sawtooth**
26	2.0 m	8.0 s	**25°**	1 day	2.0 m	8.0 s	-25°	1 day	**θ varies with cosine**
27	2.0 m	8.0 s	**35°**	1 day	2.0 m	8.0 s	-25°	1 day	**θ varies with cosine**
28	2.0 m	8.0 s	**45°**	1 day	2.0 m	8.0 s	-25°	1 day	**θ varies with cosine**
29	2.0 m	8.0 s	**55°**	1 day	2.0 m	8.0 s	-25°	1 day	**θ varies with cosine**
30	2.0 m	8.0 s	25°	**0.5 day**	2.0 m	8.0 s	-25°	1 day	
31	2.0 m	8.0 s	25°	**1.5 day**	2.0 m	8.0 s	-25°	1 day	
32	2.0 m	8.0 s	25°	**2 day**	2.0 m	8.0 s	-25°	1 day	
33	2.0 m	8.0 s	25°	**0.5 day**	2.0 m	8.0 s	-25°	**0.5 day**	
34	2.0 m	8.0 s	25°	**1.5 day**	2.0 m	8.0 s	-25°	**1.5 day**	
35	2.0 m	8.0 s	25°	**2 day**	2.0 m	8.0 s	-25°	**2 day**	
36	**1.6 m**	8.0 s	25°	1 day	2.0 m	8.0 s	-25°	1 day	
37	**1.8 m**	8.0 s	25°	1 day	2.0 m	8.0 s	-25°	1 day	
38	**2.2 m**	8.0 s	25°	1 day	2.0 m	8.0 s	-25°	1 day	
39	**2.4 m**	8.0 s	25°	1 day	2.0 m	8.0 s	-25°	1 day	
40	2.0 m	8.0 s	25°	1 day	2.0 m	8.0 s	-25°	1 day	**Strongly curved coast**
41	2.0 m	8.0 s	25°	1 day	2.0 m	8.0 s	-25°	1 day	**Gently curved coast**
42	2.0 m	8.0 s	25°	1 day	2.0 m	8.0 s	-25°	1 day	**Straight coast**
43	2.0 m	8.0 s	**-25°**	1 day	2.0 m	8.0 s	-25°	1 day	**Strongly curved coast**
44	2.0 m	8.0 s	**-25°**	1 day	2.0 m	8.0 s	-25°	1 day	**Gently curved coast**
45	2.0 m	8.0 s	**-25°**	1 day	2.0 m	8.0 s	-25°	1 day	**Straight coast**
46	2.0 m	8.0 s	**55°**	1 day	2.0 m	8.0 s	-25°	1 day	**Strongly curved coast**
47	2.0 m	8.0 s	**55°**	1 day	2.0 m	8.0 s	-25°	1 day	**Gently curved coast**
48	2.0 m	8.0 s	**55°**	1 day	2.0 m	8.0 s	-25°	1 day	**Straight coast**

Figure 1. Aerial picture of the Sand Engine in September 2014, looking in northeasterly direction. This km-scale nourishment, with 21.5 Mm^3 larger than regular nourishments (1-2 Mm^3), was constructed in July 2011 along the southwest-northeast oriented Delfland coast, The Netherlands, as a sustainable and nature-based protection measure against coastal erosion (Stive et al., 2013). Courtesy: Rijkswaterstaat, Joop van der Hout.

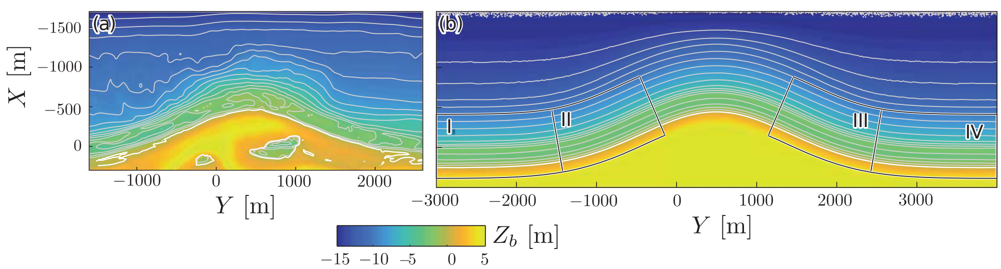

Figure 2. (a) Measured bathymetry in November 2014 at the Sand Engine (Rutten et al., 2018), and (b) synthetic bathymetry with a curved coastline and alongshore-uniform sandbar, based on measurements in (a). The black contours correspond to the boxes I-IV for the analysis of pattern growth rates.

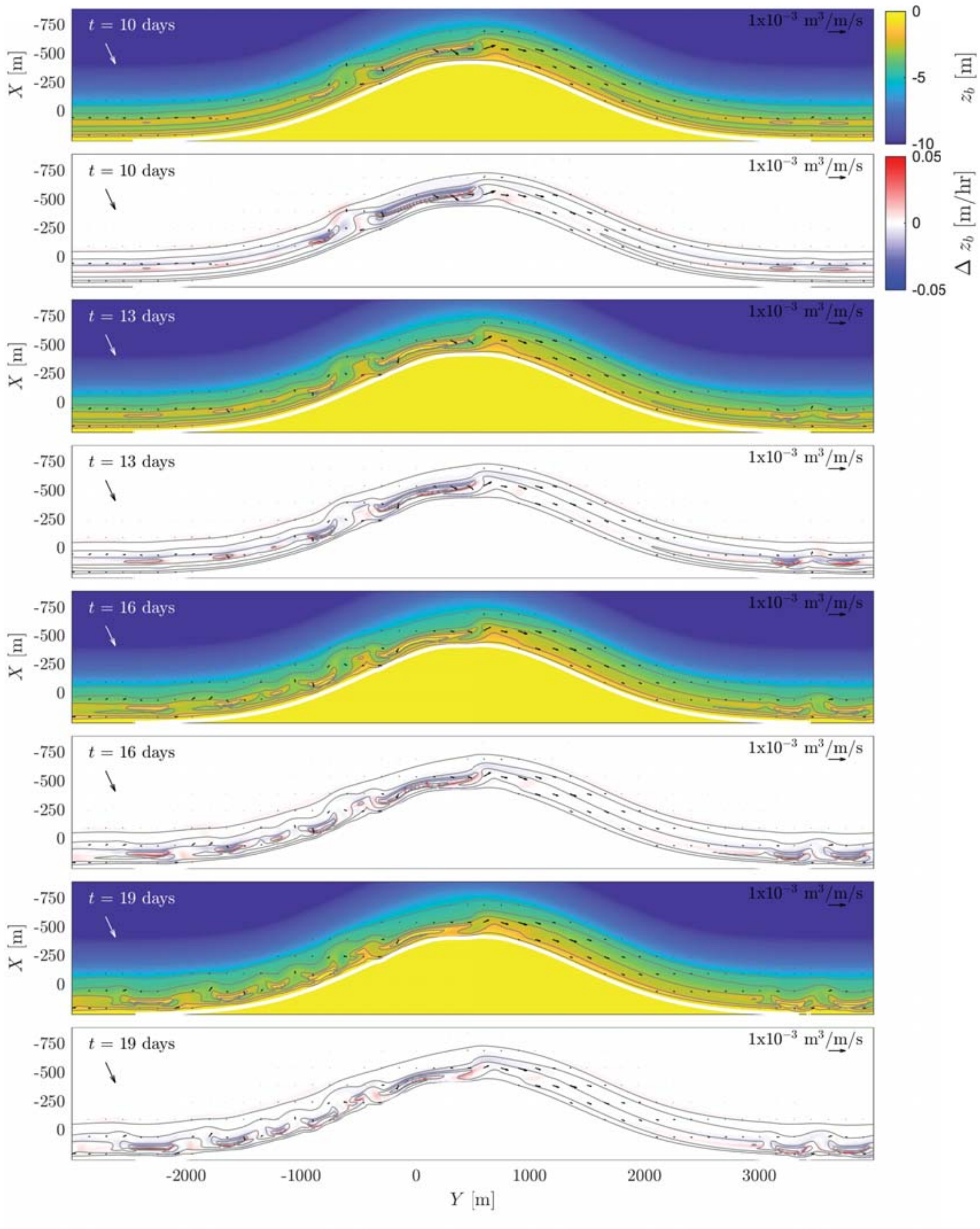

Figure 3. Bathymetric evolution (panels 1, 3, 5 and 7) and bed level change rate Δz_b (panels 2, 4, 6 and 8) of the reference scenario Ref_1. Grey lines represent the depth contours, whereas the vectors indicate the total sediment transport. The arrows in the top left corner indicate the offshore wave angle.

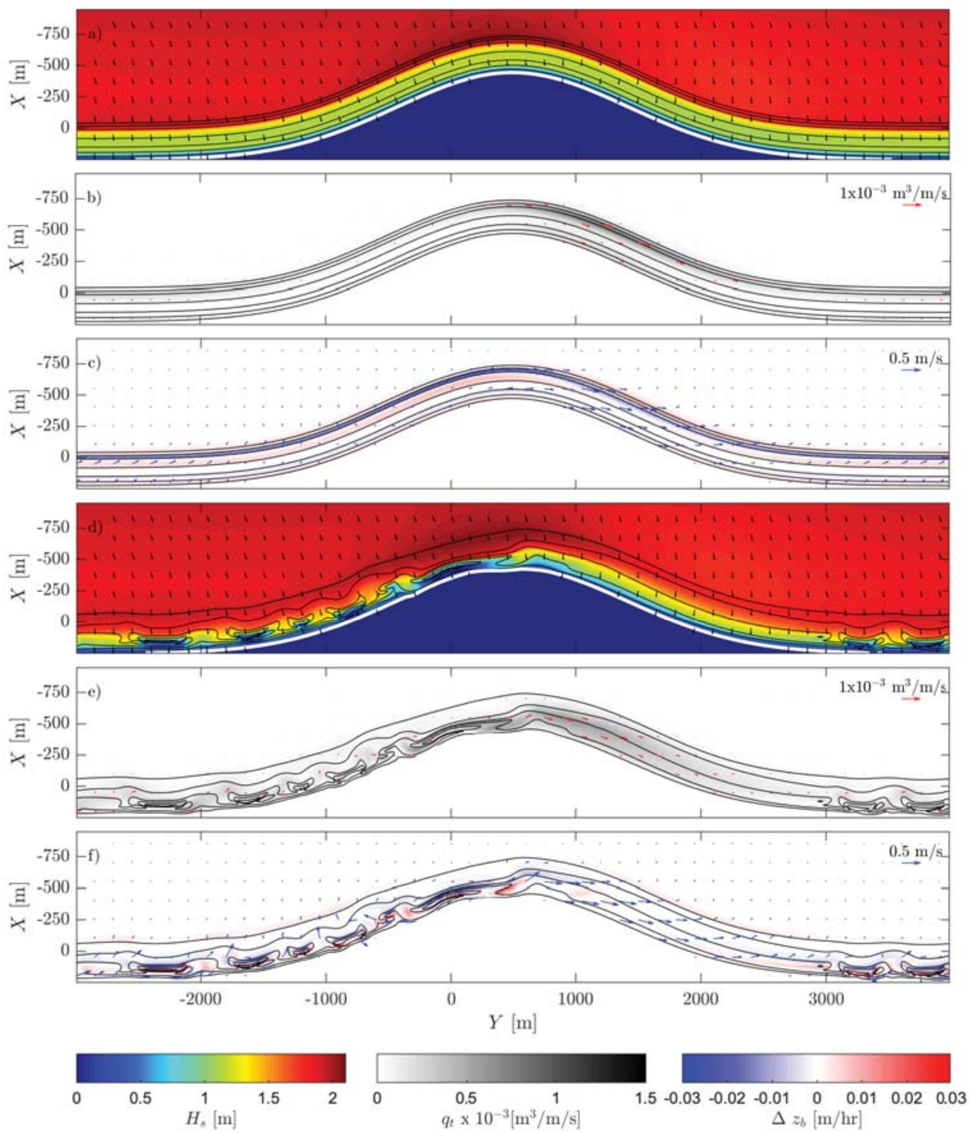

Figure 4. Patterns in (a,d) significant wave height H_s, (b,e) total sediment transport $\vec{q}_t$, and (c,f) bed level change rate Δz_b on t=0 days (a-c) and t=19 days (d-f) for the reference scenario Ref_1. Vectors indicate the wave angle (black; a-f), current velocities (blue; a,d), and total sediment transport (red; b,e), whereas the grey lines represent the depth contours.

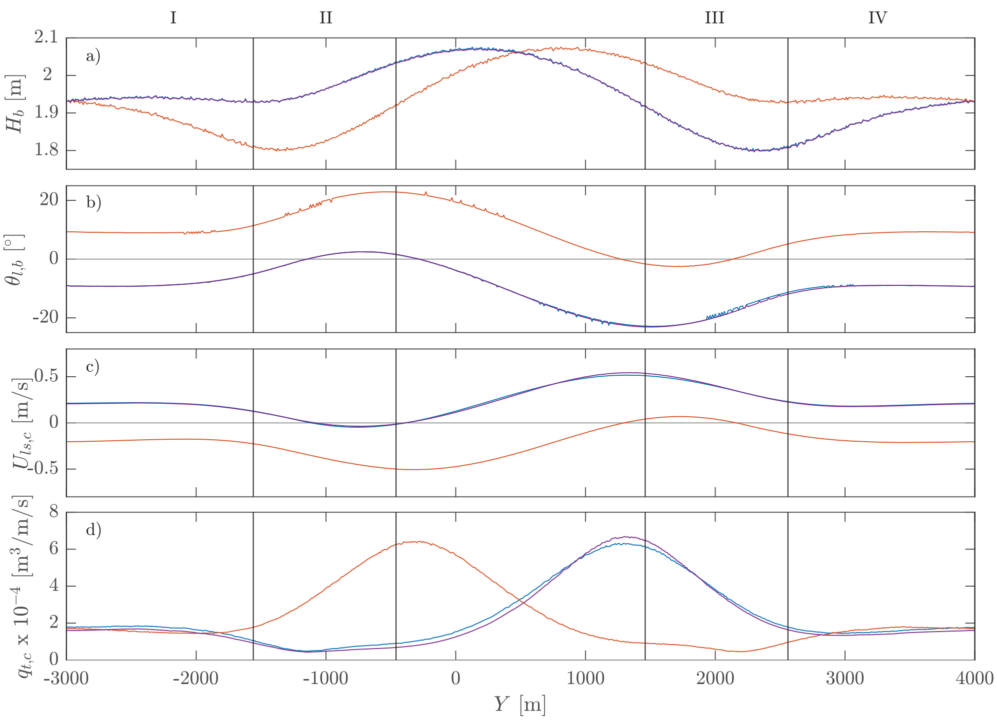

Figure 5. Alongshore variation in (a) breaker wave height H_b, (b) breaker angle $\theta_{l,b}$, (c) alongshore current at bar crest $U_{ls,c}$, and (d) total sediment transport at bar crest $\vec{q}_{t,c}$ on t=0 days (Ref_1 in blue and Ref_2 in red) and t=1 days (Ref_2 in purple). Vertical solid lines indicate sections I-IV as shown in Figure 2b.

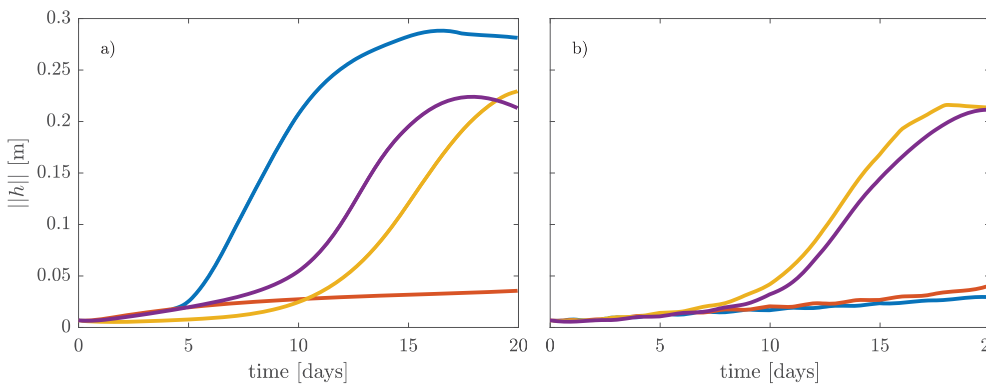

Figure 6. Time evolution of the measure for pattern amplitude $||h||$ showing the alongshore difference in growth rate of patterns in section I (yellow), section II (blue), section III (red), and section IV (purple; see Figure 2b) in reference scenario (a) Ref_1 and (b) Ref_2.

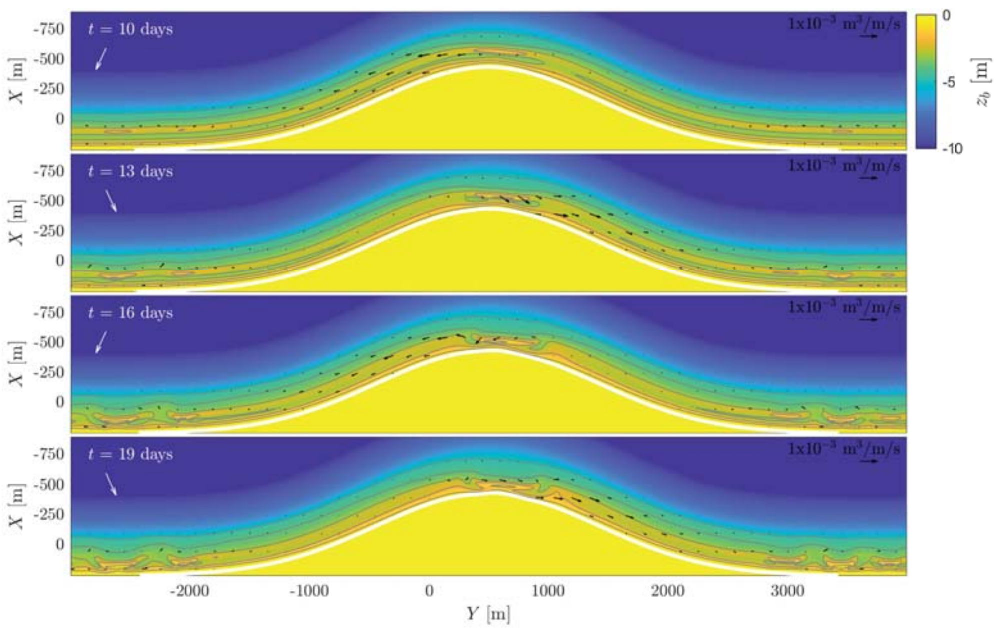

Figure 7. Bathymetric evolution of reference scenario Ref_2. Grey lines represent the depth contours, whereas the vectors indicate the total sediment transport. The arrows in the top left corner indicate the offshore wave angle.

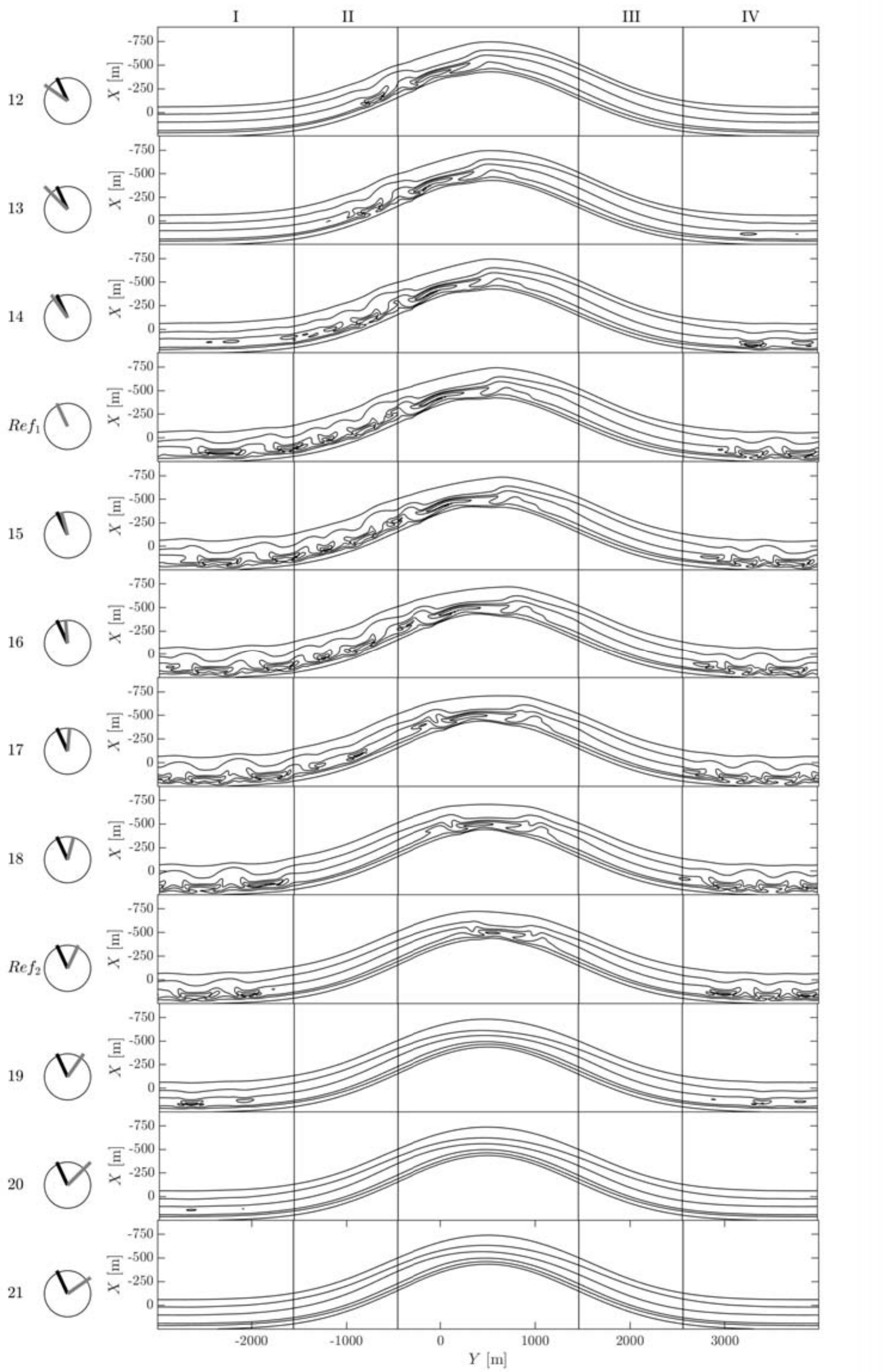

Figure 8. Bathymetric contours at $t = 19$ days for Runs 12-21, wherein θ_1 varies from -55 to 55° and θ_2 is constant at -25°. Angle variations are schematised by the circles on the left, wherein the grey and black radius indicate θ_1 and θ_2, respectively. Vertical solid lines indicate sections I-IV as shown in Figure 2b.

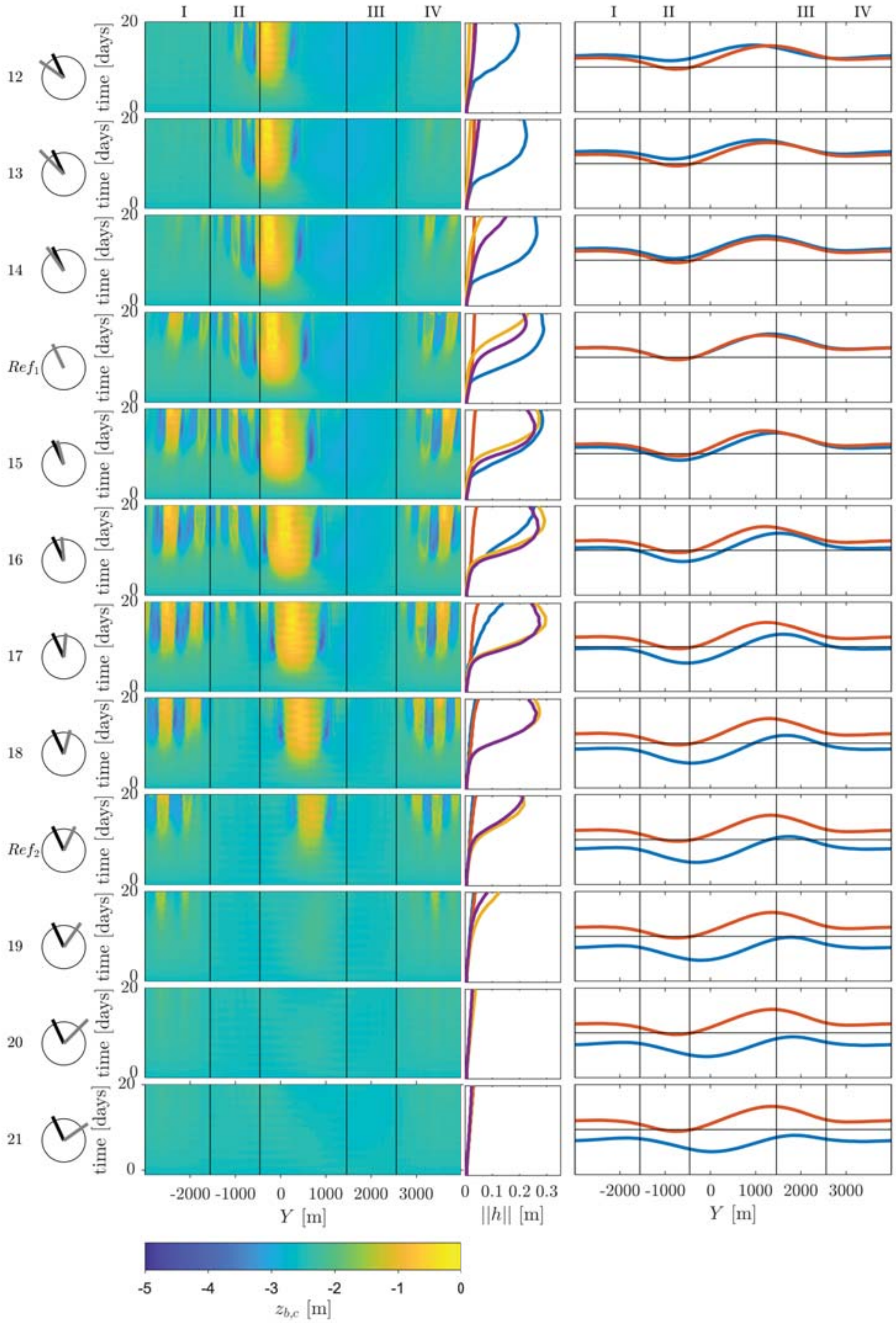

Figure 9. Simulated (left column) 20-day evolution of the bed at the bar crest $z_{b,c}$, and (right column) alongshore current at the bar crest $U_{ls,c}$ on t=0 days (blue) and t=1 days (red) versus alongshore position for Runs 12-21. Time evolution of the measure for pattern amplitude $||h||$ is shown in the middle column, for section I (yellow), section II (blue), section III (red), and section IV (purple). Angle variations are schematised by the circles on the left, wherein the grey and black radius indicate θ_1 and θ_2, respectively. Positive and negative values of $U_{ls,c}$ indicate a rightward and leftward directed current, respectively. Vertical solid lines indicate sections I-IV as shown in Figure 2b.

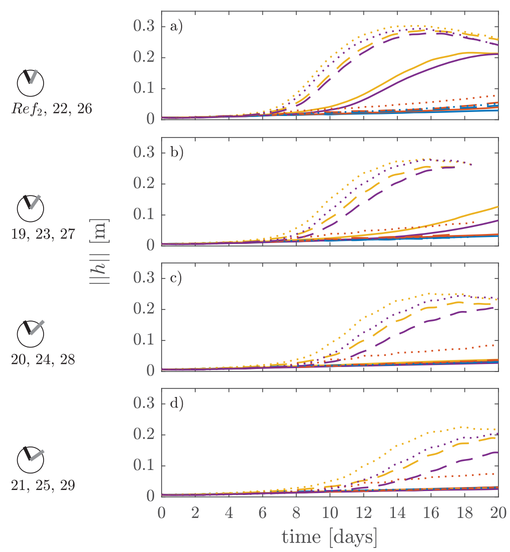

Figure 10. Time evolution of the measure for pattern amplitude $||h||$ for section I (yellow), section II (blue), section III (red), and section IV (purple). Differences in growth rate follow from varying the angle from θ_1 to θ_2 abruptly (solid lines), through a sawtooth function (dotted line) and a cosine function (dashed line). Herein, θ_1 was (a) 25°, (b) 35°, (c) 45° and (d) 55°.

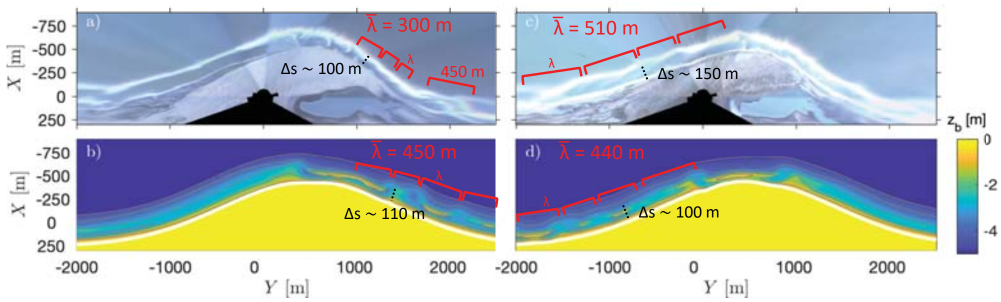

Figure 11. Comparison between (top) observations at the Sand Engine and (bottom) simulations of pattern formation under (left) time-invariant and (right) time-varying wave angle. In the 10-min averaged images the white lines, i.e. the preferencial location of wave breaking, indicate the position and planshape of the sandbar (outer line) and shoreline (inner line). Images were taken on (a) 12 March 2013 and (c) 19 November 2013. The simulations correspond to (b) Run 8 on $t = 13$ days and (d) Run 17 on $t = 19$ days. The red brackets and black dotted lines indicate the wavelength of the crescents λ, and separation distance between the bar and shoreline, respectively.

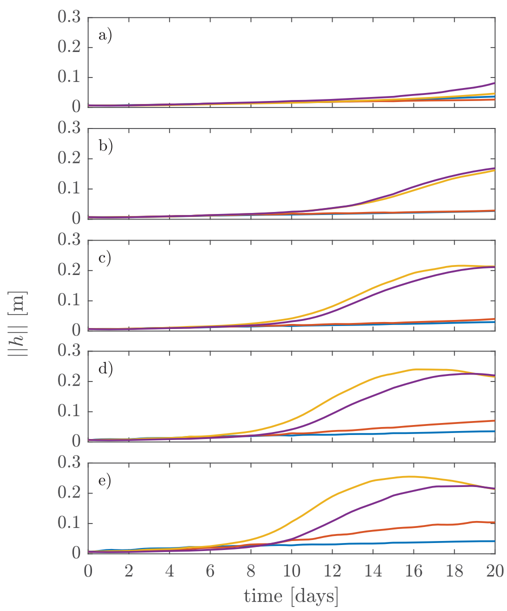

Figure 12. Time evolution of the measure for pattern amplitude $||h||$ in section I (yellow), section II (blue), section III (red), and section IV (purple; Figure 2b), for time-varying wave height H_s. Herein, $H_{s,1}$ increased from (a) 1.6 m (Run 36), to (e) 2.4 m (Run 39), while $H_{s,2} = 2.0$ m.

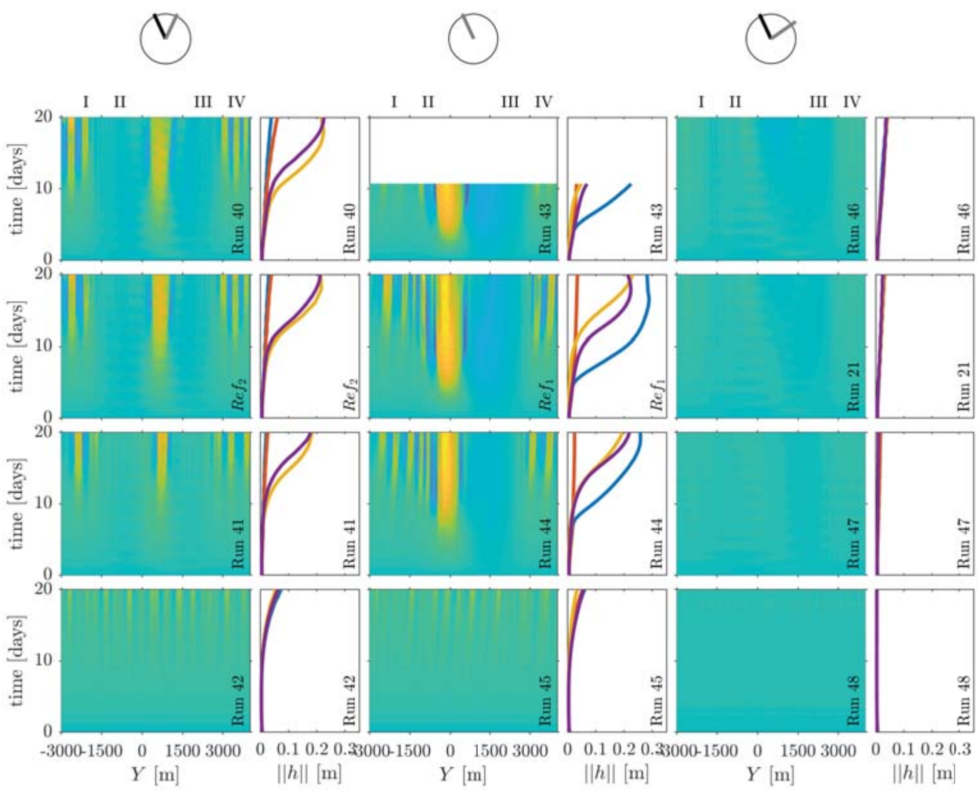

Figure 13. Simulated (column 1, 3 and 5) 20-day evolution of the bed at the bar crest $z_{b,c}$ versus alongshore position, and (column 2, 4 and 6) the measure for pattern amplitude $||h||$, for variations on the coastline curvature from strongly curved (top row) to straight (bottom row). Here, $||h||$ was computed for section I (yellow), section II (blue), section III (red), and section IV (purple), which positions are indicated in the panels with timestacks and in Figure 2b). Angle variations are schematised by the circles on the top, wherein the grey and black radius indicate θ_1 and θ_2, respectively.

Figure 1.

Figure 2.

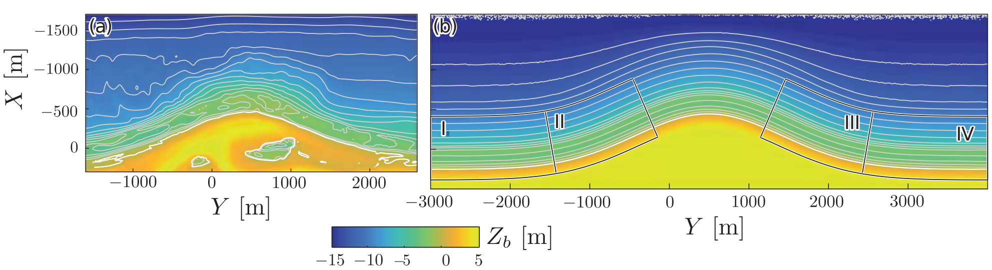
(a)
−1500
−1000
−500
0
X [m]
−1000
0
1000
2000
Y [m]
(b)
I
II
III
IV
−3000
−2000
−1000
0
1000
2000
3000
Y [m]
−15
−10
−5
0
5
Z_b [m]

Figure 3.

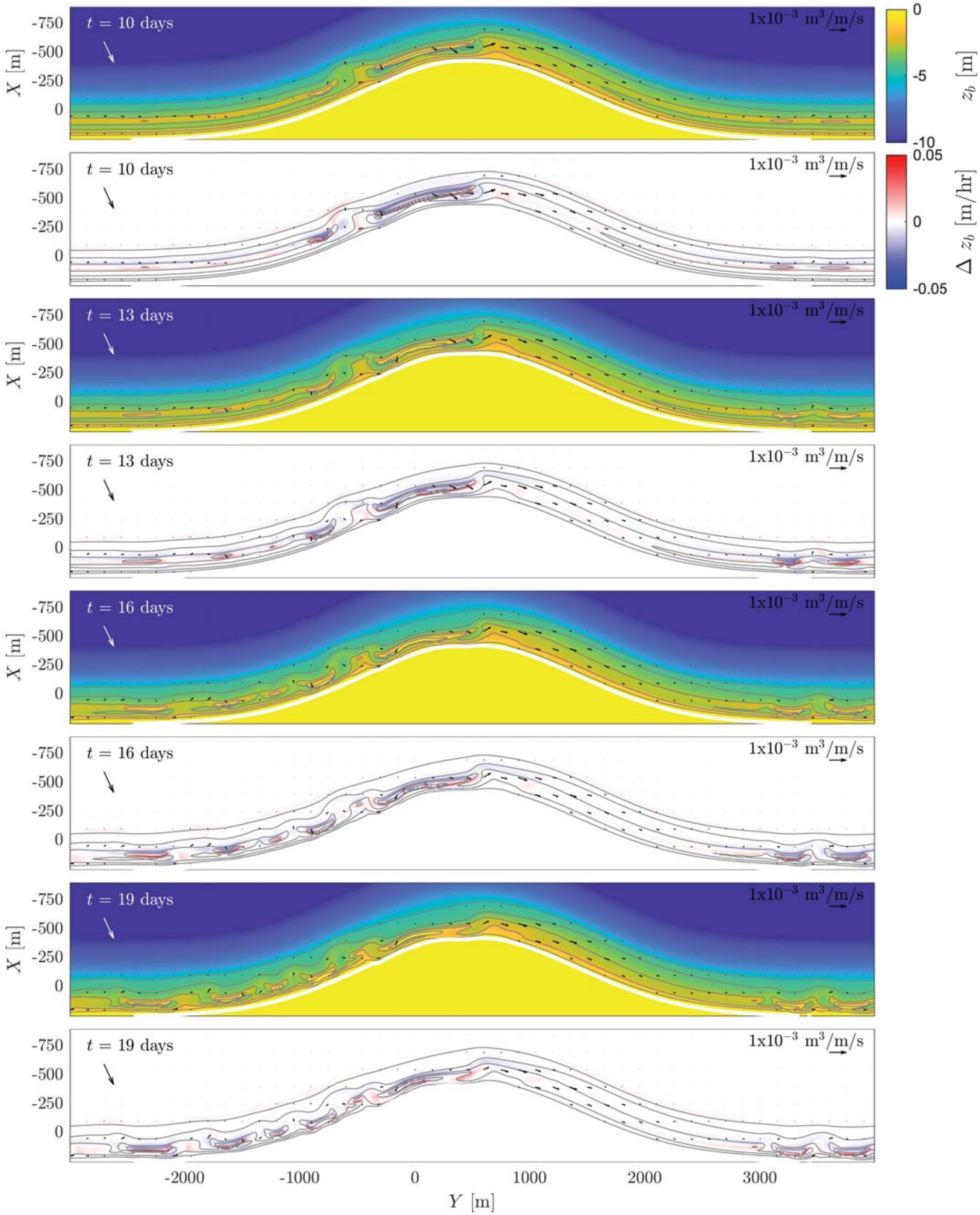

t = 10 days
t = 13 days
t = 16 days
t = 19 days
1x10^{-3} m^3/m/s
X [m]
Y [m]
z_b [m]
Δz_b [m/hr]
-750
-500
-250
0
-2000
-1000
0
1000
2000
3000
0
-5
-10
0.05
0
-0.05

Figure 4.

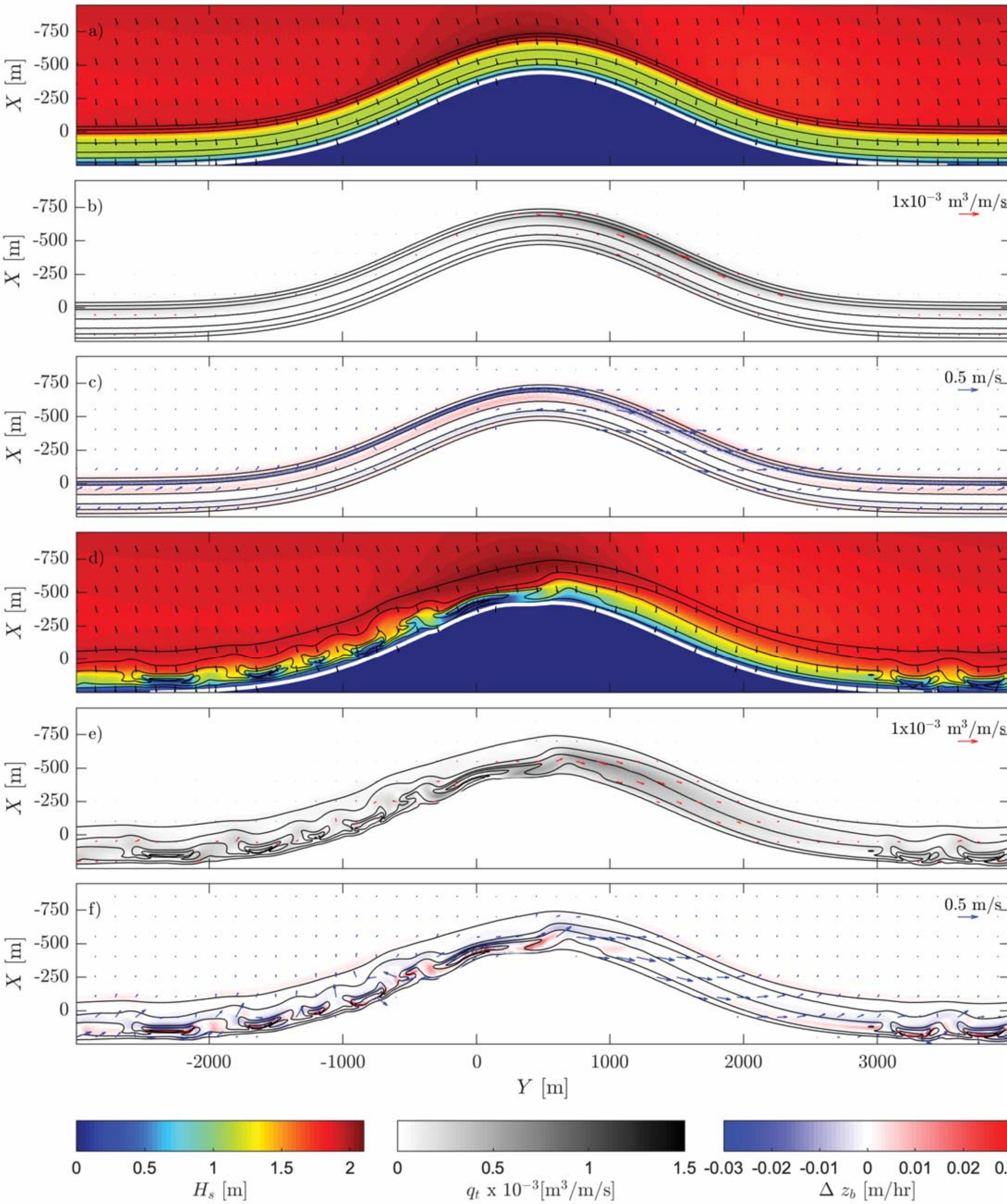

a)
b)
c)
d)
e)
f)
-750
-500
-250
0
X [m]
1x10^{-3} m^3/m/s
0.5 m/s
-2000
-1000
0
1000
2000
3000
Y [m]
0
0.5
1
1.5
2
H_s [m]
q_t x 10^{-3}[m^3/m/s]
-0.03
-0.02
-0.01
0.01
0.02
0.03
Δ z_b [m/hr]

Figure 5.

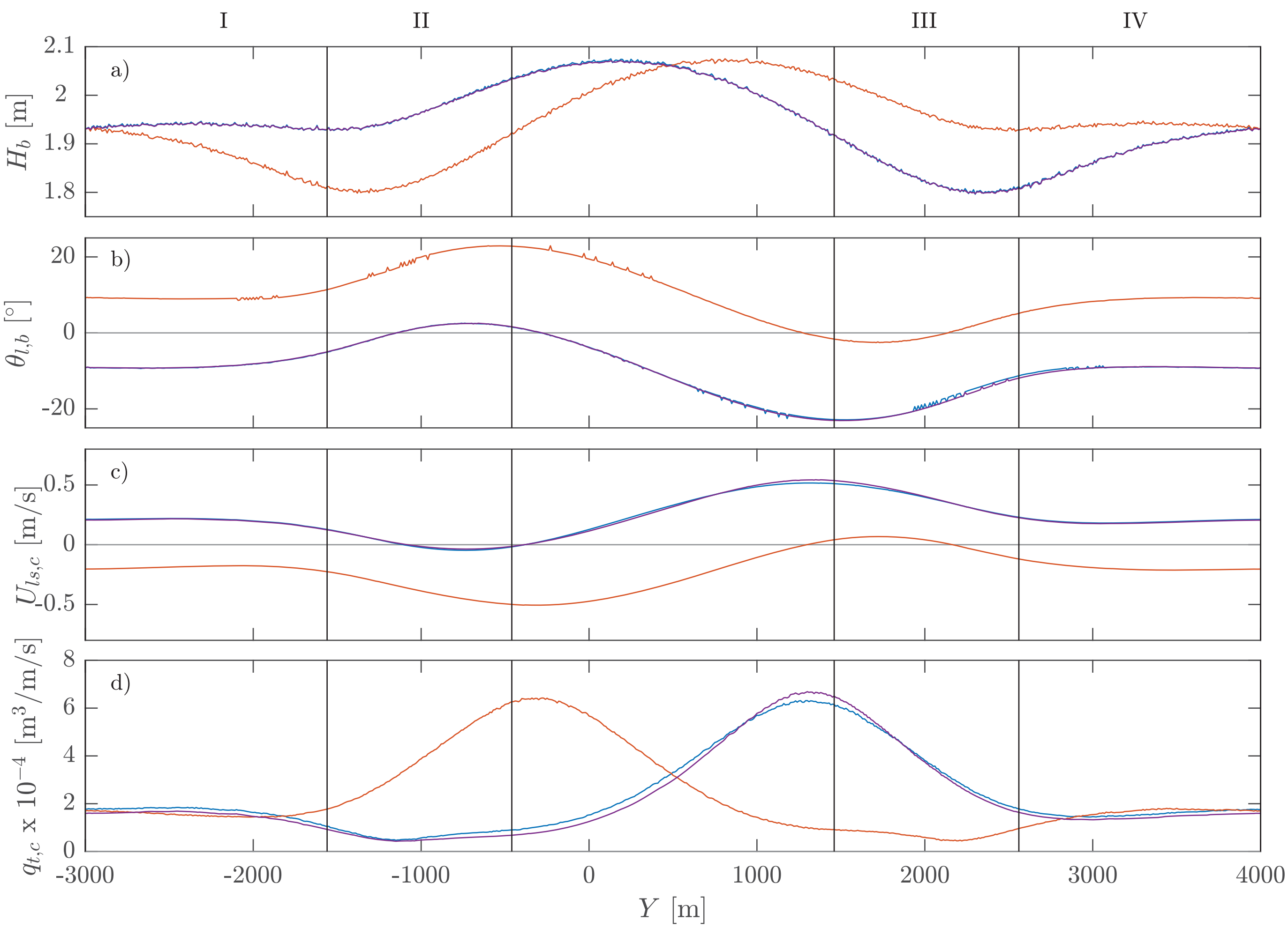

I
II
III
IV
a)
b)
c)
d)
H_b [m]
$\theta_{l,b}$ [°]
$U_{ls,c}$ [m/s]
$q_{t,c}$ x 10^{-4} [m^3/m/s]
Y [m]

Figure 6.

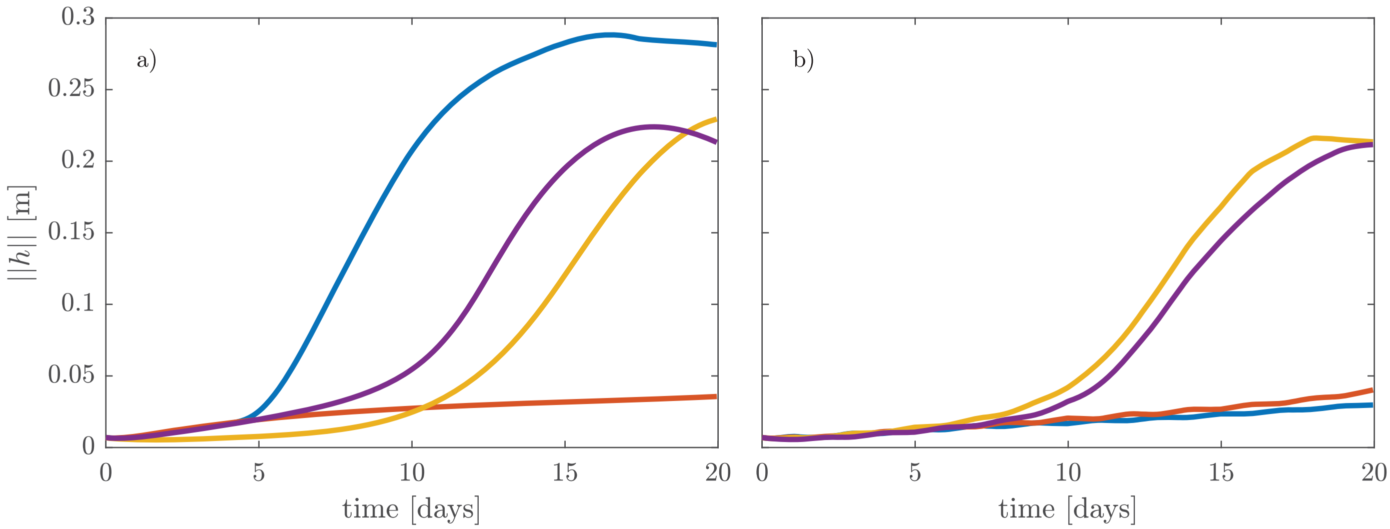

a)
b)
||h|| [m]
0
0.05
0.1
0.15
0.2
0.25
0.3
0
5
10
15
20
time [days]
time [days]

Figure 7.

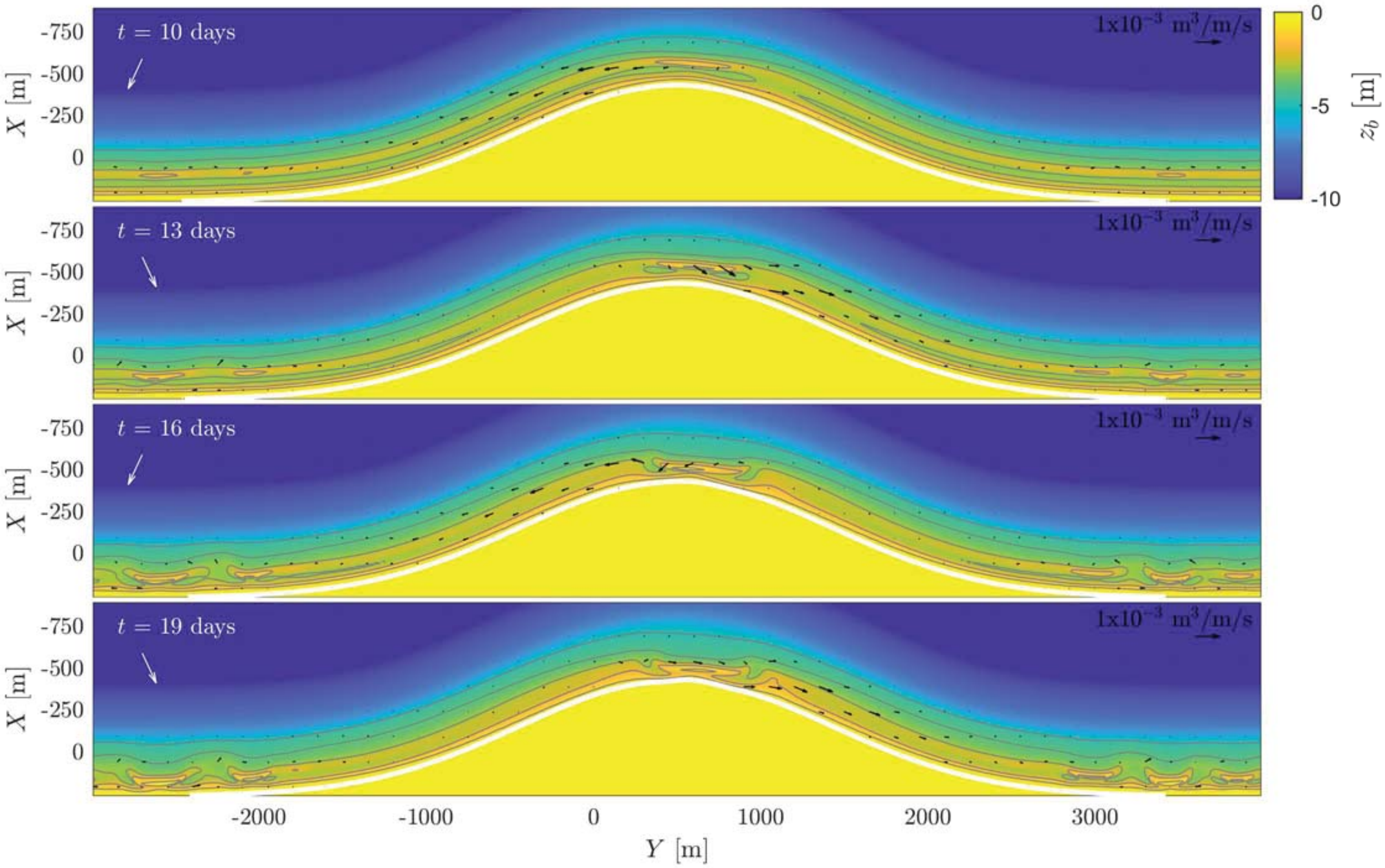

t = 10 days
t = 13 days
t = 16 days
t = 19 days
1x10^-3 m^3/m/s
X [m]
-750
-500
-250
0
Y [m]
-2000
-1000
0
1000
2000
3000
z_b [m]
0
-5
-10

Figure 8.

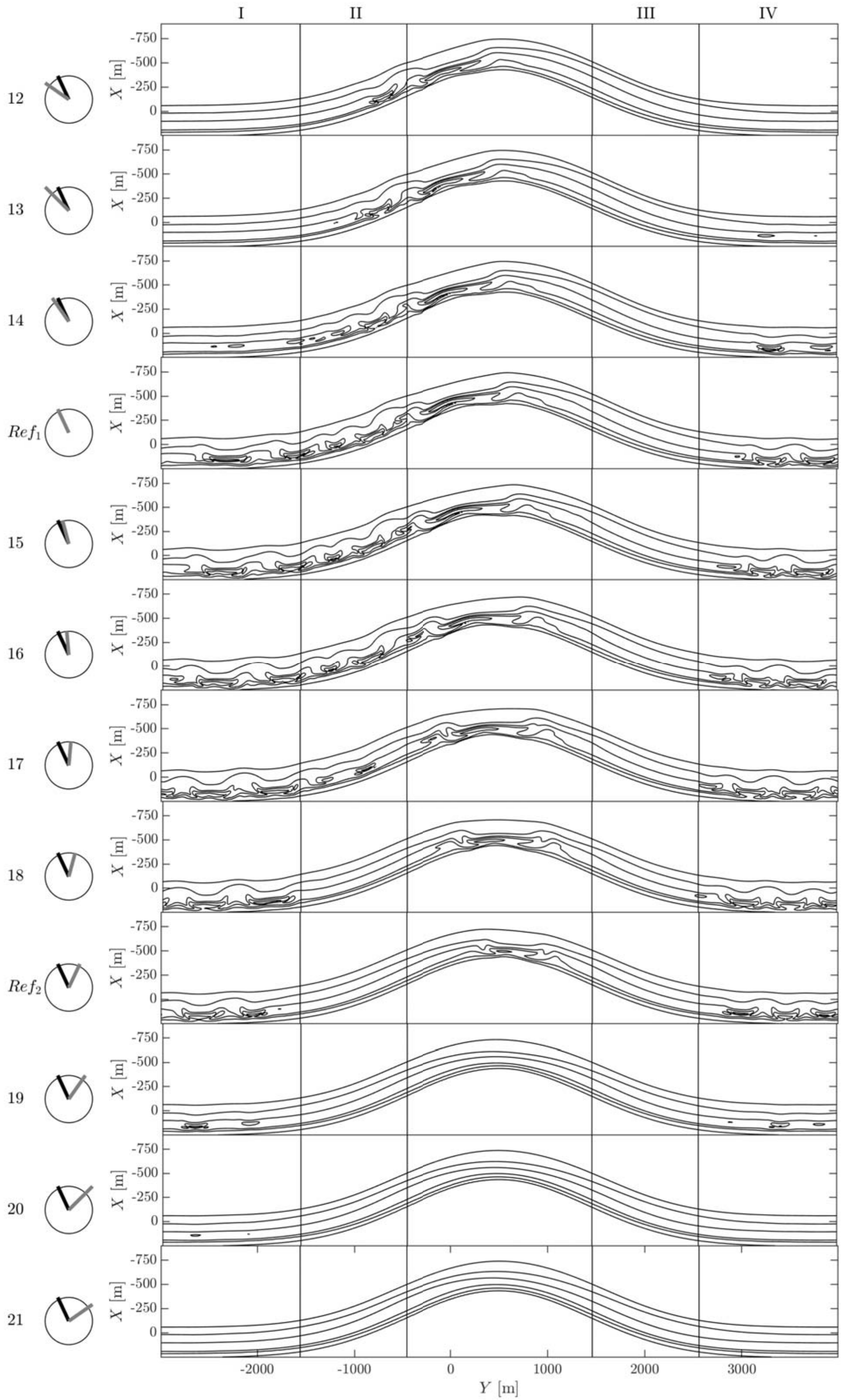

I
II
III
IV
12
13
14
Ref_1
15
16
17
18
Ref_2
19
20
21
X [m]
-750
-500
-250
0
-2000
-1000
0
1000
2000
3000
Y [m]

Figure 9.

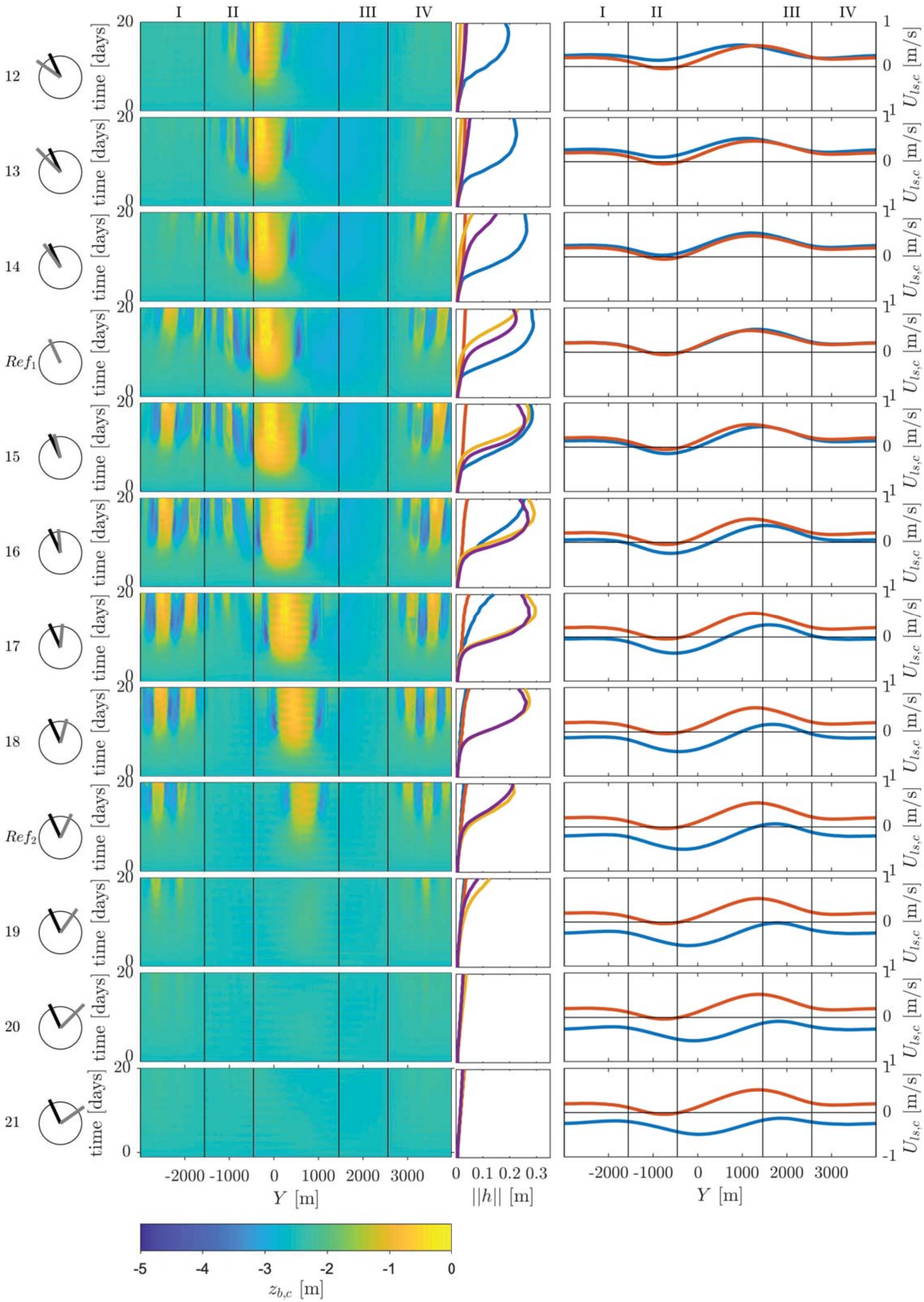

I
II
III
IV
12
13
14
Ref_1
15
16
17
18
Ref_2
19
20
21
time [days]
Y [m]
$||h||$ [m]
$U_{ls,c}$ [m/s]
$z_{b,c}$ [m]

Figure 10.

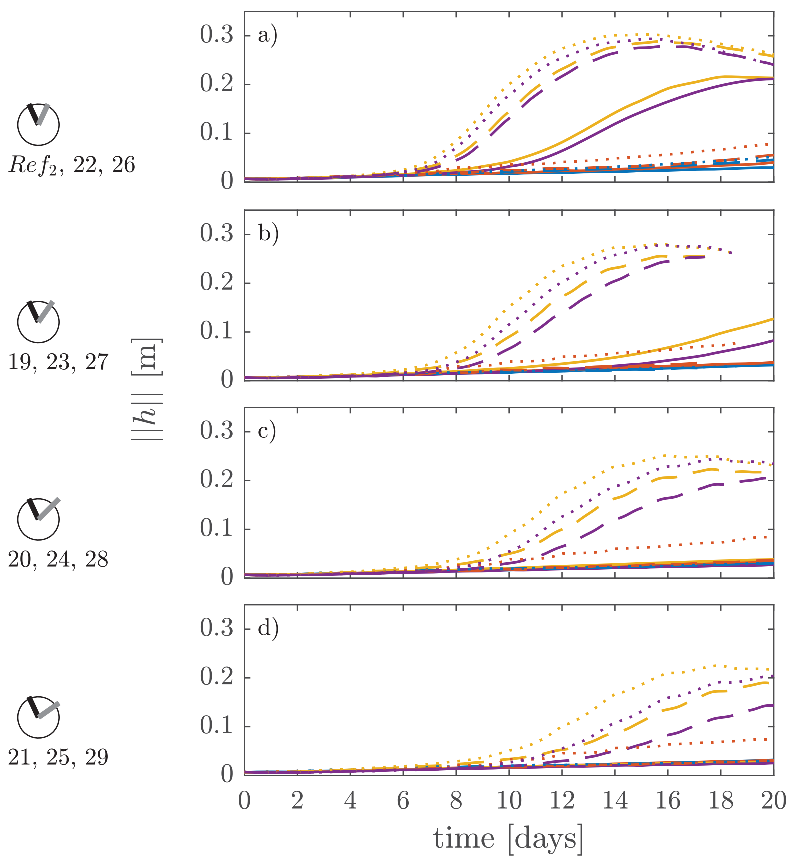

a)
b)
c)
d)
Ref_2, 22, 26
19, 23, 27
20, 24, 28
21, 25, 29
$||h||$ [m]
time [days]
0
0.1
0.2
0.3
0
2
4
6
8
10
12
14
16
18
20

Figure 11.

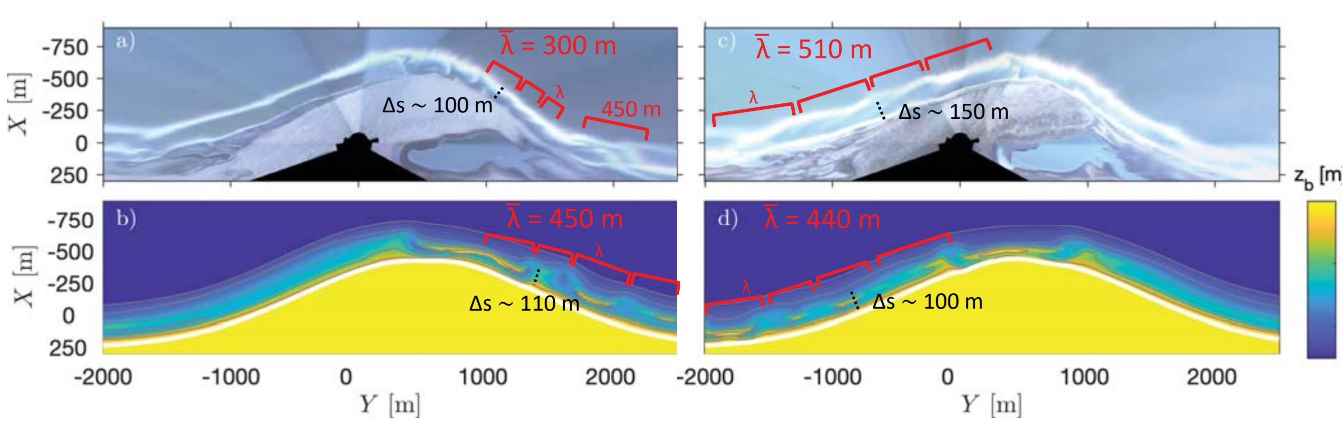

a)
$\overline{\lambda}$ = 300 m
Δs ~ 100 m
λ
450 m
c)
$\overline{\lambda}$ = 510 m
λ
Δs ~ 150 m
b)
$\overline{\lambda}$ = 450 m
λ
Δs ~ 110 m
d)
$\overline{\lambda}$ = 440 m
λ
Δs ~ 100 m
X [m]
Y [m]
z_b [m]
-750
-500
-250
0
250
-2000
-1000
0
1000
2000
-2
-4

Figure 12.

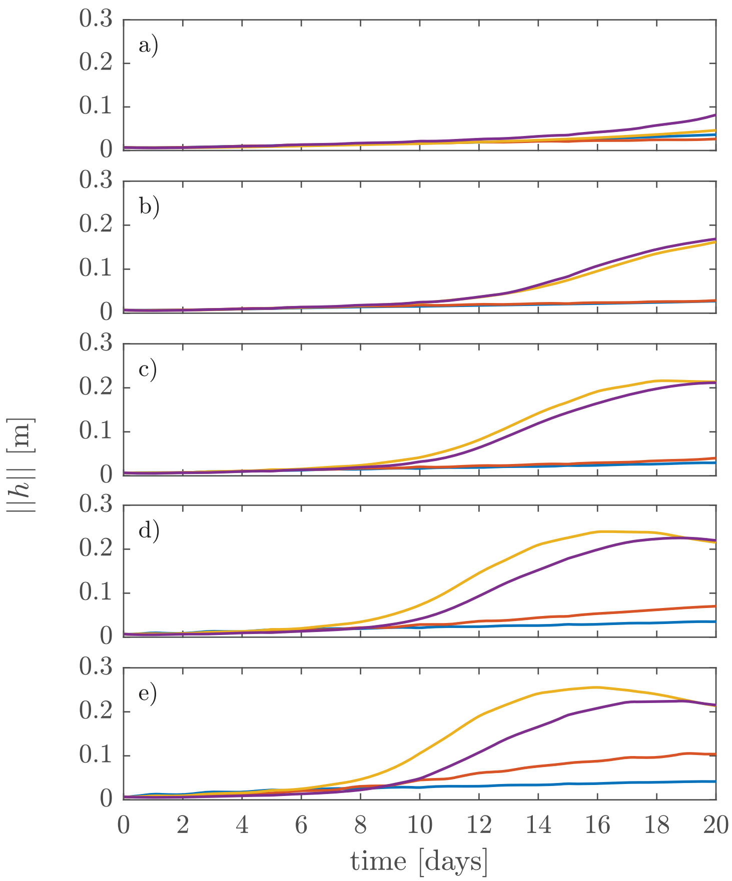

a)
b)
c)
d)
e)
||h|| [m]
time [days]

Figure 13.

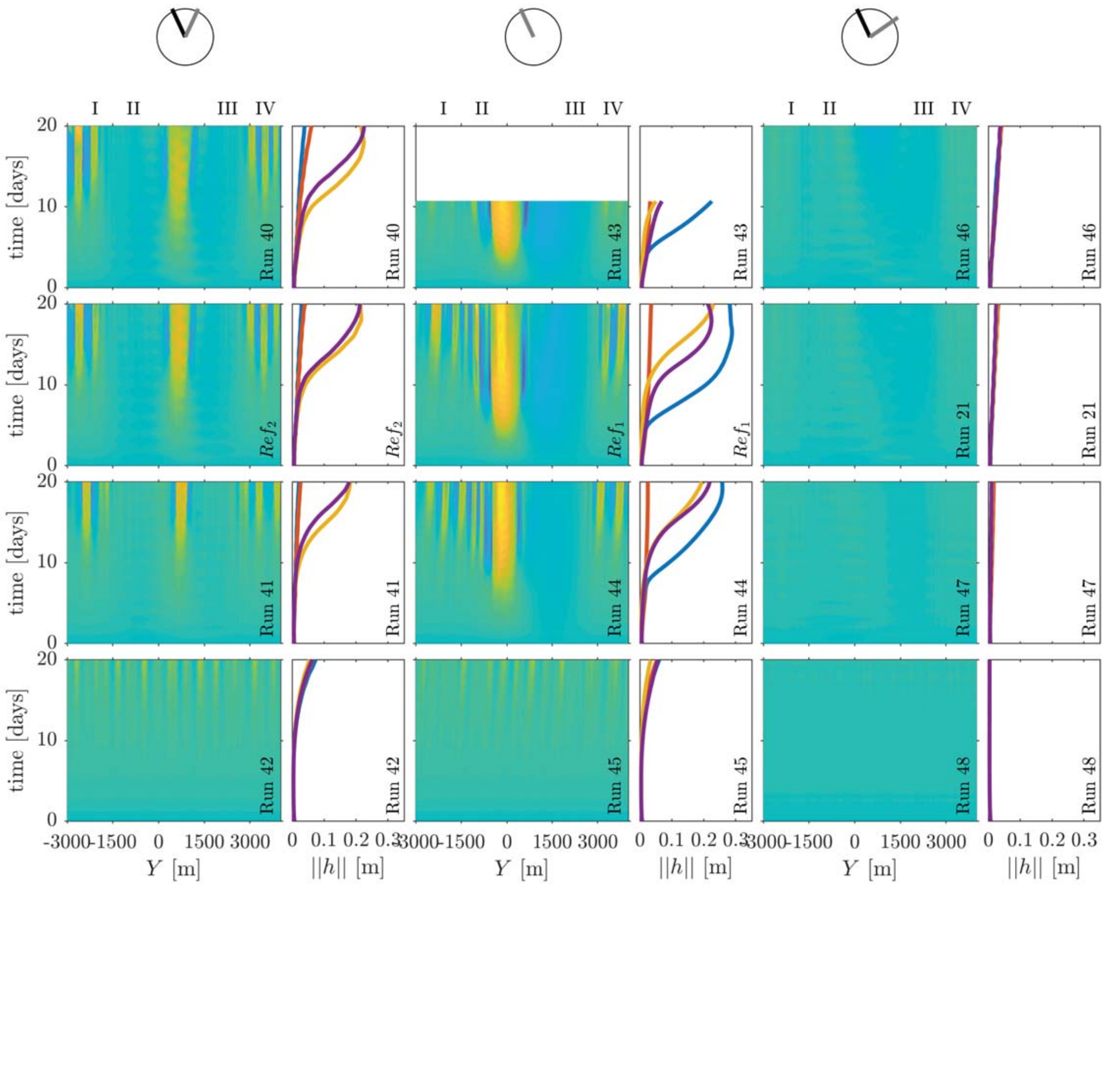

I
II
III
IV
time [days]
Run 40
Run 43
Run 46
Ref_2
Ref_1
Run 21
Run 41
Run 44
Run 47
Run 42
Run 45
Run 48
Y [m]
||h|| [m]